

A Numerical Framework for Efficient Motion Estimation on Evolving Sphere-Like Surfaces Based on Brightness and Mass Conservation Laws*

Lukas F. Lang[†]

Abstract. In this work we consider brightness and mass conservation laws for motion estimation on evolving Riemannian 2-manifolds that allow for a radial parametrization from the 2-sphere. While conservation of brightness constitutes the foundation for optical flow methods and has been generalized to said scenario, we formulate the principle of mass conservation for time-varying surfaces that are embedded in Euclidean 3-space and derive a generalized continuity equation. The main motivation for this work is efficient cell motion estimation in volumetric fluorescence microscopy images of a living zebrafish embryo. The increasing spatial and temporal resolution of modern microscopes requires efficient analysis of such data. With this application in mind we address this need and follow an emerging paradigm in this field: dimensional reduction. In light of the ill-posedness of considered conservation laws, we employ Tikhonov regularization and propose the use of spatially varying regularization functionals that recover motion only in regions with cells. For the efficient numerical solution, we devise a mesh-free Galerkin method based on compactly supported (tangent) vectorial basis functions. Furthermore, for the fast and accurate estimation of the evolving sphere-like surface from scattered data, we utilize surface interpolation with spatio-temporal regularization. We present numerical results based on the aforementioned data featuring fluorescently labeled cells.

Key words. motion estimation, optical flow, conservation laws, evolving surfaces, biomedical imaging, computer vision, continuity equation, sphere-like surfaces

AMS subject classifications. 35A15, 68U10, 92C55, 33C55, 92C37, 53A05, 65N30, 35L65

DOI. 10.1137/18M1185260

1. Introduction. Recent advances in microscopy imaging techniques allow us to study cellular dynamics of biological model organisms in more detail than ever before [29, 30, 35]. Time-lapse volumetric (4D) image sequences of the development of entire living organisms can be captured in high resolution and on a subcellular scale. However, increasing spatial and temporal resolutions require additional effort to deal with the resulting large volume of data. The need for efficient methods to analyze such data has already been acknowledged and is considered a major interdisciplinary challenge [28, 45].

One promising approach in dealing with image sequences of this type is *dimensional reduction*. A geometric model of the observed organism is introduced, and the captured data is considered only with respect to this geometry [22, 47]. These efforts focus on the true

*Received by the editors May 3, 2018; accepted for publication (in revised form) December 13, 2018; published electronically February 26, 2019.

<http://www.siam.org/journals/siims/12-1/M118526.html>

Funding: The work of the author was supported by the Leverhulme Trust project "Breaking the non-convexity barrier," EPSRC grant EP/M00493X/1, EPSRC Centre EP/N014588/1, and the Cantab Capital Institute for the Mathematics of Information.

[†]Department of Applied Mathematics and Theoretical Physics, University of Cambridge, Cambridge CB3 0WA, UK (ll542@cam.ac.uk).

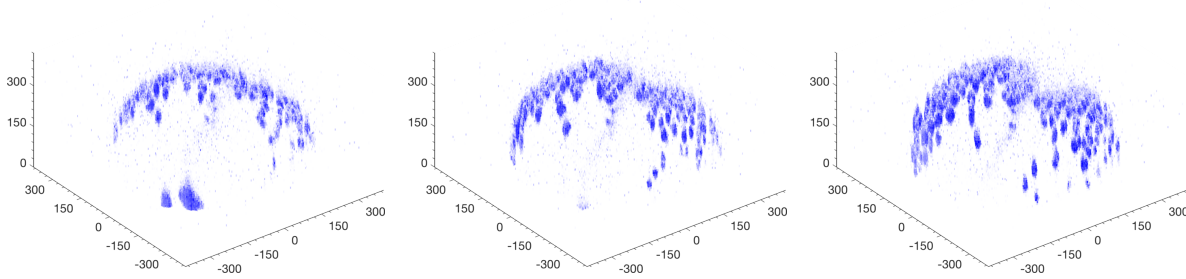


Figure 1. Frames 110, 130, 150 (left to right) of a volumetric zebrafish microscopy image sequence recorded during early embryogenesis. The sequence contains 151 frames recorded at intervals of 120 s. Blue indicates fluorescence response. As time evolves, the initially spherical yolk develops a clearly visible dent, where the embryonic axis forms and to which cells eventually converge; see also [31, Figures 11 and 15]. All dimensions are in micrometers (μm).

shape—or an approximation—of the specimen and thereby reduce the spatial dimension of the data by considering only the restriction, or a suitable projection, to this geometry. Due to the spatial sparsity of the volumetric data, the essential information is preserved.

A major gain of this approach is that it can also reduce the computational effort during analysis of the recorded material [32, 33, 34, 36, 47]. In addition, introducing a geometric representation of the specimen allows one to compute accurate measurements, such as distances, on curved surfaces rather than in—possibly distorted—projections. For the quantitative analysis of cellular processes this leads to considerable improvement [22].

The zebrafish is a popular and well-established animal research model that can be observed *in vivo*. Understanding its developmental process is of major interest. We refer the reader to [31] for a detailed discussion and illustrations. Cellular dynamics of *endodermal* cells are crucial for organ and tissue formation during early development of the organism. Despite these cells' importance, there is a lack of understanding of their migration and proliferation patterns [1, 47]. However, they are known to form a so-called *monolayer*, meaning that they do not stack on top of each other but rather float side by side forming a contiguous single-cell layer [54]. For the purpose of observation, these cells can be fluorescently labeled and recorded separately from the background by means of confocal laser-scanning microscopy. Figure 1 illustrates a section of a captured image sequence containing only the upper hemisphere of the embryo. Shown are nuclei of endodermal cells during the gastrula period forming a round surface in a single-cell layer.

The primary goal of this article is quantitative motion estimation of endodermal cells in fluorescence microscopy data of a living zebrafish embryo. Efficient motion estimation is crucial for the large-scale automated analysis of such datasets and can provide new insight into cellular mechanisms and the dynamic behavior of cells [2, 10, 41, 44, 47].

We build upon previous work [36], where the deforming single-cell layer is modeled as a closed surface $\mathcal{M}_t \subset \mathbb{R}^3$, $t \in [0, T]$, of the form $\{\tilde{\rho}(t, x)x : x \in \mathcal{S}^2\}$, together with a time-dependent function $\hat{f}(t, \cdot) : \mathcal{M}_t \rightarrow \mathbb{R}$ that indicates fluorescence response and is assumed to be directly proportional to the observed intensity. Here, $\tilde{\rho}(t, \cdot) : \mathcal{S}^2 \rightarrow (0, \infty)$ is a radial

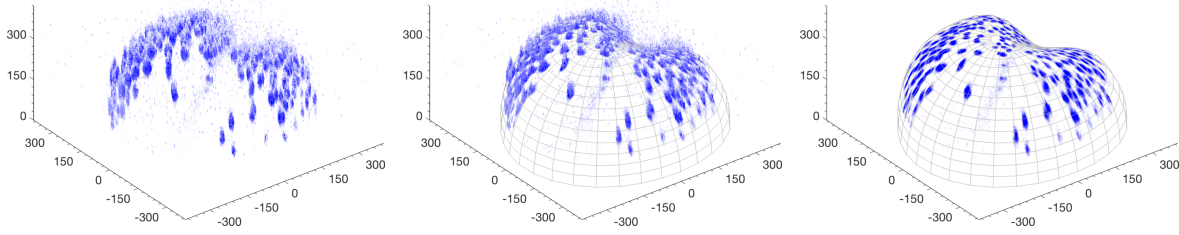


Figure 2. Frame 150 of the zebrafish image sequence. The left image depicts the unprocessed volumetric microscopy data f^δ . The curved mesh in the center image illustrates a sphere-like surface fitted to approximate cell centers. The right image shows the surface data \hat{f} obtained by taking the radial maximum intensity projection of f^δ onto the surface within a narrow band. For details see section 5. All dimensions are in micrometers (μm).

deformation of the 2-sphere \mathcal{S}^2 . See Figure 2 for the general idea and Figure 3 for a sketch.

The main idea, which was developed in [32, 34], is to conceive the motion of a cell as it migrates through Euclidean 3-space only with respect to this moving surface. As a consequence, the velocity $\hat{\mathbf{U}}(t, x) \in \mathbb{R}^3$ of a cell that always stays on this surface can be decomposed into the sum of a—prescribed and in general not tangential—surface velocity $\hat{\mathbf{V}}(t, x) \in \mathbb{R}^3$ and a purely tangential velocity $\hat{\mathbf{w}}(t, x) \in \mathbb{R}^3$ that is relative to $\hat{\mathbf{V}}$. See Figure 3 for an illustration. Consequently, one can estimate $\hat{\mathbf{w}}$ from the data \hat{f} by solving a parametrized optical flow problem

$$d_t^{\hat{\mathbf{V}}} \hat{f} + \nabla_{\mathcal{M}} \hat{f} \cdot \hat{\mathbf{w}} = 0$$

on this evolving surface. Here, $d_t^{\hat{\mathbf{V}}}$ denotes a suitable temporal derivative, $\nabla_{\mathcal{M}}$ the (spatial) gradient, and a dot the standard inner product. As a result, the velocity of a cell can be estimated as $\hat{\mathbf{U}} = \hat{\mathbf{V}} + \hat{\mathbf{w}}$. While $\hat{\mathbf{w}}$ is relative to the chosen $\hat{\mathbf{V}}$ and should be interpreted with care, it is reasonable to assume that their sum is close to the true velocity of a cell.

In this model, \hat{f} is assumed to satisfy a *brightness constancy assumption*, which is typical for optical flow-based motion estimation: the intensity \hat{f} is conserved along trajectories of moving points. However, in many situations it is too restrictive and possibly violated; see, e.g., the discussion in [14, sect. 3]. In this article, we address this issue and assume that \hat{f} instead fulfills *conservation of mass*. We derive a suitable generalization of the continuity equation to evolving surfaces which are embedded in \mathbb{R}^3 and obtain the pointwise conservation law

$$d_t^{\hat{\mathbf{N}}} \hat{f} + \nabla_{\mathcal{M}} \cdot (\hat{f} \hat{\mathbf{u}}) - \hat{f} KV = 0.$$

Here, $d_t^{\hat{\mathbf{N}}}$ denotes the normal time derivative and $\nabla_{\mathcal{M}} \cdot$ the divergence, K is related to surface curvature, and V is the scalar normal velocity of the moving surface. The main advantage of this formulation, compared to [32, 34, 36], is that one is able to directly infer the entire tangential velocity $\hat{\mathbf{u}} = \text{P}_{\mathcal{M}}(\hat{\mathbf{U}})$ of cells from the data \hat{f} , where $\text{P}_{\mathcal{M}}$ denotes the orthogonal projector onto the tangent space of \mathcal{M}_t . The normal component of $\hat{\mathbf{U}}$ is prescribed by the

surface's normal velocity, and the total velocity $\hat{\mathbf{U}}$ can thus be estimated by adding the tangential part $\hat{\mathbf{u}}$.

In view of the ill-posedness of the above-mentioned conservation equations, we follow a variational approach. While dense motion estimation is often desired for complex natural scenes, it is redundant for the aforementioned microscopy data. Such data is considerably simpler due to the characteristic shape of cell nuclei, the absence of occlusions, and its sparsity. In order to mitigate undesired fill-in effects of quadratic regularization functionals to areas where \hat{f} is zero, we introduce novel regularization functionals inspired by image segmentation models; see, e.g., [7]. Given a segmentation of the cells, motion is only estimated in regions where data is present.

1.1. Contributions. The contributions of this article are as follows. First, we introduce the concepts of brightness and mass conservation laws on evolving surfaces and discuss how they relate to each other. While conservation of brightness is the foundation for the optical flow equation and has been dealt with in [32, 34, 36], in this article we generalize the principle of mass conservation to time-varying surfaces that are embedded in Euclidean 3-space and derive a generalized continuity equation.

Second, we propose new spatially varying regularization functionals for motion estimation based on the discussed conservation laws. They are specifically tailored to the mentioned fluorescence microscopy data and indicate motion only in regions where cells are present.

Third, for the numerical solution, we propose a mesh-free Galerkin method based on compactly supported (vectorial) basis functions. Resulting sparsity effects lead to vast improvements in performance compared to [36], which uses globally supported basis functions. Moreover, we provide a formula for the Hilbert–Schmidt norm of the covariant derivative of a vector field, which is commonly used for (quadratic) tangent vector field regularization. As a result, the Gram–Schmidt orthonormalization of the tangent basis is rendered redundant, yielding another major performance gain compared to [8, 34, 36].

Fourth, for extracting a sphere-like surface, together with surface image data, from the aforementioned microscopy image sequences we propose surface interpolation with spatio-temporal regularization. Compared to [36], where only spatial regularization is used, this leads to a more accurate estimation of the surface's (normal) velocity and the surface data, which in turn should improve the accuracy of the computed cell velocities.

Fifth, we present numerical results based on the aforementioned zebrafish microscopy data. We compute and compare cell motion estimated by imposing either of the two discussed conservation laws.

1.2. Related work. Concerning dense motion estimation in \mathbb{R}^2 , Horn and Schunck [26] were the first to propose a variational approach based on conservation of brightness. They minimize a Tikhonov-type functional with H^1 Sobolev seminorm regularization. For a general introduction to the topic see [4, 5], and for a survey on various optical flow functionals see [55]. Well-posedness of the Horn–Schunck functional is proved in [48], where the problem is treated on irregular planar domains and solved by means of a finite element method. In [57], an extension to the domain $[0, T] \times \mathbb{R}^2$, including spatial as well as temporal first-order regularization, is proposed. A framework unifying various spatial and temporal regularizers can be found in [56]. For the comparison of different motion estimation methods, an evaluation framework is developed in [6].

It is only recently that generalizations to non-Euclidean and nonstatic domains have received increasing attention. For the purpose of robot vision, optical flow on the static round sphere is considered in [27, 52]. With an application to brain image analysis, [39] generalizes the Horn–Schunck functional to static surfaces that are embedded in \mathbb{R}^3 and proves well-posedness. Numerically, the problem is solved on a triangle mesh with a finite element method.

With the aim of analyzing cell motion in fluorescence microscopy data, [32, 34] consider a generalization of the Horn–Schunck functional to evolving surfaces with boundary. In particular, [34] proposes a generalization of the spatio-temporal model in [57]. Minimization is performed by solving the associated Euler–Lagrange equations in the coordinate domain with a finite-difference scheme. In [33], several decomposition models for optical flow on the static 2-sphere are studied and solved by means of projection to finite-dimensional spaces spanned by tangent vector spherical harmonics. In [8], optical flow on moving manifolds with and without spatial boundary is investigated. That work considers product manifolds for which an appropriate Riemannian metric is constructed and well-posedness is shown. In [36], the embryo of a zebrafish is modeled as an evolving sphere-like surface. The generalized optical flow problem is solved by means of a Galerkin method based on tangent vector spherical harmonics. In order to find the sphere-like surface from microscopy data, surface interpolation from approximate cell centers is proposed.

We also refer the reader to [2, 41, 44], where optical flow is computed to track cells in microscopy data, and to [10], where it is used to infer the motion of neural crest cells in zebrafish microscopy images. Moreover, in [47] the sphere is used to model the embryo of a zebrafish, and the motion of endodermal cells is computed in map projections by means of fluid image registration.

According to [14], Schunck [50] was the first work to propose motion estimation in image sequences based on the continuity equation. Since then it has been used in numerous works, as mass preservation is a particularly appealing alternative for fluid motion estimation. See, for instance, [3, 9, 13, 14, 15, 16, 23, 51, 59, 60].

Finally, for mesh-based numerical methods for the solution of partial differential equations on static and on evolving surfaces, see [46] and [19], respectively.

The remainder of this article is structured as follows. In section 2, we introduce sphere-like evolving surfaces and vectorial Sobolev spaces on manifolds. In section 3, we discuss brightness and mass conservation on evolving surfaces and introduce a variational formulation for each conservation principle. Section 4 is dedicated to their numerical solution based on compactly supported (vectorial) basis functions. We derive necessary and sufficient conditions. In order to find a sphere-like surface from the data, we propose surface interpolation with spatio-temporal regularization and discuss its numerical solution by means of scalar spherical harmonics. In section 5, we discuss, compare, and visualize numerical results based on the aforementioned microscopy data. Section 6 concludes the article.

2. Notation and background.

2.1. Sphere-like surfaces. We consider closed smooth 2-manifolds $\mathcal{M}_t \subset \mathbb{R}^3$ which are embedded in the 3-dimensional Euclidean space and are indexed by time $t \in I$, where $I := [0, T] \subset \mathbb{R}$ is a time interval. Each \mathcal{M}_t is assumed to be regular and oriented by the outward

unit normal field $\hat{\mathbf{N}}(t, x) \in \mathbb{R}^3$, $x \in \mathcal{M}_t$. Its total curvature $K(t, x)$, which is twice the mean curvature, is defined as $K(t, x) = (-\nabla_{\mathbb{R}^3} \cdot \hat{\mathbf{N}})(t, x)$, where $\nabla_{\mathbb{R}^3} \cdot$ denotes the usual divergence of the embedding space.

Let us assume that the family $\mathcal{M} = \{\mathcal{M}_t\}_{t \in I}$ admits a smooth and smoothly evolving parametrization of the form

$$(2.1) \quad \mathbf{y} : I \times \Omega \rightarrow \mathbb{R}^3, \quad (t, \xi^1, \xi^2)^\top \mapsto \tilde{\rho}(t, \mathbf{x}(\xi^1, \xi^2))\mathbf{x}(\xi^1, \xi^2) \in \mathcal{M}_t.$$

Here, $\mathbf{x} : \Omega \subset \mathbb{R}^2 \rightarrow \mathbb{R}^3$ denotes a regular parametrization of the 2-sphere $\mathcal{S}^2 = \{x \in \mathbb{R}^3 : \|x\| = 1\}$, mapping points $\xi = (\xi^1, \xi^2)^\top \in \Omega$ in the coordinate domain to points $x = (x^1, x^2, x^3)^\top \in \mathcal{S}^2$ on the sphere, and $\tilde{\rho} : I \times \mathcal{S}^2 \rightarrow (0, \infty)$ denotes a sufficiently regular (radius) function. Moreover, $\|x\| = \sqrt{x \cdot x}$ denotes the norm of \mathbb{R}^n , $n = \{2, 3\}$. We refer to \mathcal{M} as an *evolving sphere-like surface*. Figure 3 illustrates the setting.

Let us denote by $\hat{f} : \mathcal{M} \rightarrow \mathbb{R}$ a smooth function on \mathcal{M} , by $f : I \times \Omega \rightarrow \mathbb{R}$ its coordinate representation, and by $\tilde{f} : I \times \mathcal{S}^2 \rightarrow \mathbb{R}$ its representation on \mathcal{S}^2 . For $t \in I$ and $\xi \in \Omega$, they are related by

$$(2.2) \quad f(t, \xi) = \tilde{f}(t, \mathbf{x}(\xi)) = \hat{f}(t, \mathbf{y}(t, \xi)).$$

Functions that are defined on \mathcal{S}^2 are indicated with a tilde, whereas functions defined on \mathcal{M} are indicated with a hat. Their coordinate representation is treated without special indication. The partial derivative with respect to ξ^i is abbreviated as ∂_i . Accordingly, the partial derivative with respect to time is denoted by ∂_t . Moreover, we define a smooth (spatial) extension \bar{f} of \hat{f} to $\mathbb{R} \setminus \{0\}$ as

$$(2.3) \quad \bar{f}(t, x) = \hat{f} \left(t, \tilde{\rho} \left(t, \frac{x}{\|x\|} \right) \frac{x}{\|x\|} \right).$$

It is constant along radial lines and coincides with $\tilde{f}(t, \cdot)$ on \mathcal{S}^2 and with $\hat{f}(t, \cdot)$ on \mathcal{M}_t , respectively. In the following, we assume time $t \in I$ arbitrary but fixed. Moreover, since $\tilde{\rho} \equiv 1$ gives $\mathcal{M}_t = \mathcal{S}^2$, for all $t \in I$, we introduce the following concepts only for \mathcal{M}_t .

The tangent space at a point $\mathbf{y}(t, \xi) \in \mathcal{M}_t$, $\xi \in \Omega$, is denoted by $T_{\mathbf{y}(t, \xi)}\mathcal{M}_t \subset T_{\mathbf{y}(t, \xi)}\mathbb{R}^3$ and is defined in terms of derivations of smooth functions on \mathcal{M}_t ; see [37, Chap. 2]. The tangent bundle is defined by $T\mathcal{M}_t = \{\{\mathbf{y}(t, \xi)\} \times T_{\mathbf{y}(t, \xi)}\mathcal{M}_t : \xi \in \Omega\}$. The orthogonal projector onto the tangent space $T_x\mathcal{M}_t$ at $x \in \mathcal{M}_t$ is given by

$$(2.4) \quad P_{\mathcal{M}}(t, x) = \text{Id} - \hat{\mathbf{N}}(t, x)\hat{\mathbf{N}}(t, x)^\top \in \mathbb{R}^{3 \times 3}.$$

Similarly, $T_{\mathbf{x}(\xi)}\mathcal{S}^2$ and $T\mathcal{S}^2$ (respectively, $T_\xi\Omega$ and $T\Omega$) are defined.

The parametrization (2.1) gives rise to the differential $D\mathbf{y}(t, \xi) : T_\xi\Omega \rightarrow T_{\mathbf{y}(t, \xi)}\mathcal{M}_t$ at $\xi \in \Omega$ and provides a unique identification of a tangent vector field \mathbf{v} on Ω with a tangent vector field $\hat{\mathbf{v}}$ on \mathcal{M}_t via $\hat{\mathbf{v}}(\mathbf{y}(t, \xi)) = D\mathbf{y}(t, \xi)(\mathbf{v}(\xi))$. Moreover, the parametrization naturally induces a Riemannian metric g on the coordinate domain by means of the pullback metric. For tangent vectors $\mathbf{u}, \mathbf{v} \in T_\xi\Omega$, $\xi \in \Omega$, this metric is given by

$$(2.5) \quad \langle \mathbf{u}, \mathbf{v} \rangle_g := (\mathbf{y}(t, \xi))^* \langle \cdot, \cdot \rangle_{\mathbb{R}^3}(\mathbf{u}, \mathbf{v}) = D\mathbf{y}(t, \xi)(\mathbf{u}) \cdot D\mathbf{y}(t, \xi)(\mathbf{v}).$$

Similarly, \mathbf{x} gives rise to $D\mathbf{x}$, which identifies \mathbf{v} with $\tilde{\mathbf{v}}$. The Riemannian metric for \mathcal{S}^2 is defined accordingly.

The spatial gradient $\nabla_{\mathbb{R}^2} f$ of a smooth function f in the coordinate domain is the unique vector field that satisfies $\nabla_{\mathbb{R}^2} f(t, \xi) \cdot \mathbf{v}(\xi) = df(t, \xi)(\mathbf{v}(\xi))$ for all $\mathbf{v} \in T\Omega$, where $df(\mathbf{v})$ denotes the directional derivative of f in direction \mathbf{v} . Consequently, for a smooth function \hat{f} as in (2.2) the gradient $\nabla_{\mathcal{M}} \hat{f}$ is defined via

$$(2.6) \quad \nabla_{\mathcal{M}} \hat{f}(t, x) \cdot \hat{\mathbf{v}}(x) = d\hat{f}(t, x)(\hat{\mathbf{v}}(x)) \quad \forall \hat{\mathbf{v}} \in T\mathcal{M}_t,$$

where $d\hat{f}(t, x)(\hat{\mathbf{v}}(x))$ is the directional derivative of $\hat{f}(t, x)$ at $x \in \mathcal{M}_t$ in the direction of the tangent vector $\hat{\mathbf{v}}(x)$. The gradient $\nabla_{\mathcal{S}^2} \tilde{f}$ is defined analogously. Let us emphasize that, for an arbitrary extension such as, e.g., (2.3), the gradient is just the tangential component of the usual gradient of the embedding space, i.e.,

$$\nabla_{\mathcal{M}} \hat{f}(t, x) = (\mathbb{P}_{\mathcal{M}} \nabla_{\mathbb{R}^3} \bar{f})(t, x).$$

Consequently, we can consider coordinate vector fields $\partial_i \mathbf{y}(t, \xi)$, $i \in \{1, 2\}$. At a point $\mathbf{y}(t, \xi) \in \mathcal{M}_t$, the set $\{\partial_1 \mathbf{y}(t, \xi), \partial_2 \mathbf{y}(t, \xi)\}$ forms a basis for the tangent space $T_{\mathbf{y}(t, \xi)} \mathcal{M}_t$. A tangent vector $\hat{\mathbf{v}} \in T_{\mathbf{y}(t, \xi)} \mathcal{M}_t$ can thus be uniquely represented as $\hat{\mathbf{v}} = \sum_{i=1}^2 v^i \partial_i \mathbf{y}(t, \xi)$, with $\mathbf{v} = (v^1, v^2)^\top \in \mathbb{R}^2$ its coordinate representation. The elements v^i are called components of $\hat{\mathbf{v}}$. We will use the Einstein summation convention and sum over each index letter appearing exactly twice in an expression, once as a subscript and once as a superscript. For instance, we will write $\hat{\mathbf{v}} = v^i \partial_i \mathbf{y}$ for the sake of brevity. As a further notational convention, boldface letters are used to denote vector fields. In particular, lowercase boldface letters refer to tangent vector fields, whereas uppercase boldface letters refer to general vector fields in \mathbb{R}^3 , with the exception of the parametrizations \mathbf{x} and \mathbf{y} . Moreover, we will drop arguments, such as (t, ξ) or (t, x) , whenever they are clear from the context.

Having defined coordinate vector fields we find, by application of the product and the chain rule to (2.1), that

$$D\mathbf{y} = (\partial_1 \mathbf{y} \quad \partial_2 \mathbf{y}) = ((\partial_1 \rho) \mathbf{x} \quad (\partial_2 \rho) \mathbf{x}) + \rho D\mathbf{x} \in \mathbb{R}^{3 \times 2},$$

where $D\mathbf{x} = (\partial_1 \mathbf{x} \quad \partial_2 \mathbf{x})$ and $\rho : I \times \Omega \rightarrow (0, \infty)$ is the coordinate representation of $\tilde{\rho}$. By (2.5), the components $g_{ij} = \partial_i \mathbf{y} \cdot \partial_j \mathbf{y}$ of the Riemannian metric $g \in \mathbb{R}^{2 \times 2}$ are given by

$$g = \begin{pmatrix} (\partial_1 \rho)^2 & \partial_1 \rho \partial_2 \rho \\ \partial_2 \rho \partial_1 \rho & (\partial_2 \rho)^2 \end{pmatrix} + \rho^2 D\mathbf{x}^\top D\mathbf{x},$$

and the elements of the inverse g^{-1} are denoted by (g^{ij}) . For further details on the concepts discussed above we refer the reader to standard differential geometry books, such as [17, 18, 37, 38].

2.2. Vectorial Sobolev spaces on manifolds. For arbitrary but fixed $t \in I$, the surface integral of a function \hat{f} , as defined in (2.2), is given by

$$(2.7) \quad \int_{\mathcal{M}_t} \hat{f} \, d\mathcal{M}_t = \int_{\Omega} f J\mathbf{y} \, d\xi,$$

where $(J\mathbf{y})^2 = \det(g)$ is the Jacobian of \mathbf{y} ; see Theorem 3 in [18, p. 88].

For a tangent vector field $\hat{\mathbf{v}}$, we denote by $\nabla_{\hat{\mathbf{u}}}\hat{\mathbf{v}}(t, x)$ the covariant derivative at a point $x \in \mathcal{M}_t$ along a tangent vector $\hat{\mathbf{u}} \in T_x\mathcal{M}_t$; cf. [37, Chaps. 4 and 5]. Given a componentwise extension $\bar{\mathbf{v}}$ of $\hat{\mathbf{v}}$ to \mathbb{R}^3 , it is the tangential part of the usual directional derivative of $\bar{\mathbf{v}}$ in direction $\hat{\mathbf{u}}$ in the embedding space, that is,

$$\nabla_{\hat{\mathbf{u}}}\hat{\mathbf{v}}(t, x) = (\mathbb{P}_{\mathcal{M}}\nabla_{\mathbb{R}^3}\bar{\mathbf{v}}(\hat{\mathbf{u}}))(t, x).$$

The covariant derivative is a linear operator $\nabla\hat{\mathbf{v}}(t, x) : T_x\mathcal{M}_t \rightarrow T_x\mathcal{M}_t$, and its Hilbert–Schmidt norm is given by

$$(2.8) \quad \|\nabla\hat{\mathbf{v}}(t, x)\|_2^2 = \sum_{i=1}^2 \|\nabla_{\hat{\mathbf{e}}_i}\hat{\mathbf{v}}(t, x)\|^2,$$

where $\{\hat{\mathbf{e}}_1, \hat{\mathbf{e}}_2\}$ is an arbitrary orthonormal basis of the tangent space $T_x\mathcal{M}_t$. We highlight that (2.8) is invariant with regard to the chosen parametrization \mathbf{y} . Moreover, the divergence $\nabla_{\mathcal{M}} \cdot \hat{\mathbf{v}}$ of a tangent vector field $\hat{\mathbf{v}}$ is defined by

$$\nabla_{\mathcal{M}} \cdot \hat{\mathbf{v}} = \text{Tr}(\nabla\hat{\mathbf{v}}) = \sum_{i=1}^2 \nabla_{\hat{\mathbf{e}}_i}\hat{\mathbf{v}} \cdot \hat{\mathbf{e}}_i.$$

For each $t \in I$, we define the Sobolev space $H^1(\mathcal{M}_t, T\mathcal{M}_t)$ as the completion of all $C^\infty(\mathcal{M}_t, T\mathcal{M}_t)$ tangent vector fields with respect to

$$(2.9) \quad \|\hat{\mathbf{v}}(t, \cdot)\|_{H^1(\mathcal{M}_t, T\mathcal{M}_t)}^2 := \int_{\mathcal{M}_t} \|\nabla\hat{\mathbf{v}}(t, x)\|_2^2 d\mathcal{M}_t.$$

Note that (2.9) is a norm whenever \mathcal{M}_t is diffeomorphic to the 2-sphere since, by virtue of the hairy ball theorem, no covariantly constant tangent vector field but $\hat{\mathbf{v}} = 0$ exists [25, p. 125]. We refer the reader to [21, 53] for more details on Sobolev spaces on Riemannian manifolds.

3. Problem formulation. Let us consider an evolving sphere-like surface

$$(3.1) \quad \mathcal{M} := \bigcup_{t \in I} (\{t\} \times \mathcal{M}_t) \subset \mathbb{R}^4,$$

which is specified in terms of a parametrization $\mathbf{y} : I \times \Omega \rightarrow \mathbb{R}^3$ as in (2.1). Every choice of \mathbf{y} gives rise to a surface velocity

$$(3.2) \quad \hat{\mathbf{V}}(t, x) = \partial_t \mathbf{y}(t, \xi) \in \mathbb{R}^3,$$

where $\xi = \mathbf{y}^{-1}(t, x)$. We stress that the velocity $\hat{\mathbf{V}}$ depends on the chosen parametrization \mathbf{y} of which, in general, infinitely many exist. However, its (scalar) normal component, given by

$$V = \hat{\mathbf{V}} \cdot \hat{\mathbf{N}},$$

is intrinsic and thus independent of the choice of \mathbf{y} ; see [34, Prop. 1]. As a consequence, (3.2) can be represented as

$$(3.3) \quad \hat{\mathbf{V}} = V\hat{\mathbf{N}} + \hat{\mathbf{v}},$$

where $V\hat{\mathbf{N}}$ is the normal velocity and $\hat{\mathbf{v}}$ is a vector field tangent to \mathcal{M}_t , $t \in I$.

In the following, we consider smooth trajectories of moving particles (or cells) which always stay on the evolving surface. To this end, we assume the existence of a Lagrangian specification

$$(3.4) \quad \gamma(\cdot, x) : t \mapsto \gamma(t, x) \in \mathcal{M}_t, \quad \gamma(0, \cdot) = \text{Id},$$

of the path of a particle. Expressing (3.4) with the help of a coordinate representation $\beta : I \times \Omega \rightarrow \Omega$ requires that

$$(3.5) \quad \gamma(t, \mathbf{y}(0, \xi)) = \mathbf{y}(t, \beta(t, \xi)), \quad \beta(0, \cdot) = \text{Id},$$

hold for all $(t \times \xi) \in I \times \Omega$. As a consequence of (3.5) and with the help of (3.2) we find that

$$(3.6) \quad \begin{aligned} \partial_t \gamma &= \partial_t \mathbf{y} + \partial_t \beta^i \partial_i \mathbf{y}, \\ &= \hat{\mathbf{V}} + \hat{\mathbf{w}}, \end{aligned}$$

where $\hat{\mathbf{w}} = \partial_t \beta^i \partial_i \mathbf{y}$ is a purely tangential velocity. Therefore, the velocity of a particle moving along (3.4) can be decomposed into the surface velocity $\hat{\mathbf{V}}$, which is prescribed by the chosen parametrization \mathbf{y} , and a tangential part $\hat{\mathbf{w}}$ relative to it. See Figure 3 for a sketch.

As a consequence of (3.4) and (3.5) we infer that the normal part of the velocity of a particle following γ equals the normal velocity of the surface movement. In other words,

$$\begin{aligned} \partial_t \gamma \cdot \hat{\mathbf{N}} &= (\hat{\mathbf{V}} + \hat{\mathbf{w}}) \cdot \hat{\mathbf{N}} \\ &= \hat{\mathbf{V}} \cdot \hat{\mathbf{N}} \\ &= V. \end{aligned}$$

Suppose now that the evolving surface (3.1) is embedded in a fluid which moves with a velocity $\mathbf{U}(t, x) \in \mathbb{R}^3$, $x \in \mathbb{R}^3$. For $t \in I$ and $x \in \mathcal{M}_t$, we denote the restriction of $\mathbf{U}(t, x)$ to the surface \mathcal{M}_t by $\hat{\mathbf{U}}(t, x)$. We stress that this fluid velocity is in general different from the surface velocity $\hat{\mathbf{V}}$ defined in (3.2).

In the following we assume that a particle of interest following (3.4) convects with this fluid. In other words, for $t \in I$ and $x \in \mathcal{M}_t$ we require that

$$(3.7) \quad \hat{\mathbf{U}}(t, x) = \partial_t \gamma(t, \gamma^{-1}(t, x)).$$

From (3.6) and (3.3) we find that

$$(3.8) \quad \begin{aligned} \hat{\mathbf{U}} &= \hat{\mathbf{V}} + \hat{\mathbf{w}} \\ &= V\hat{\mathbf{N}} + \hat{\mathbf{v}} + \hat{\mathbf{w}}. \end{aligned}$$

Therefore, the surface (3.1) must evolve with (scalar) normal velocity $V = \hat{\mathbf{U}} \cdot \hat{\mathbf{N}}$. Since the fluid velocity $\hat{\mathbf{U}}$ can uniquely be decomposed into a normal and a tangential part, we conclude that the latter is given by

$$(3.9) \quad \hat{\mathbf{u}} = \hat{\mathbf{v}} + \hat{\mathbf{w}}.$$

The primary goal of this article is to estimate the motion of cells as they move along trajectories (3.4) through Euclidean 3-space. The main assumption is that they form a surface structure which is deforming over time and can be estimated from data \hat{f} . Hence, we focus on estimating $\hat{\mathbf{U}}$ rather than \mathbf{U} and use the fact that the unknown can be decomposed as in (3.8). In the following we discuss two conceptually different ways of estimating the tangential part of the particle motion. One is based on conservation of the data \hat{f} along paths (3.4) and leads to a generalized optical flow equation [32, 34]. The other idea is based on conservation of mass and leads to a suitable generalization of the continuity equation to evolving surfaces.

3.1. Conservation of brightness. Let us be given a function \hat{f} such that, for time $t \in I$,

$$\hat{f}(t, \cdot) : \mathcal{M}_t \rightarrow \mathbb{R}$$

is an image on the surface \mathcal{M}_t . In this section we assume that, along a smooth trajectory (3.4), this data \hat{f} satisfies

$$(3.10) \quad \hat{f}(t, \gamma(t, x)) = \hat{f}(0, x)$$

for all $t \in I$ and all $x \in \mathcal{M}_0$. Typically, this constraint is termed the *brightness constancy assumption* and is the basis for many motion estimation methods.

In order to linearize (3.10) by differentiation with respect to time, one may consider temporal derivatives along trajectories; see [32, 34]. To this end, we define the time derivative of \hat{f} along a trajectory $\psi : t \mapsto \psi(t) \in \mathcal{M}_t$ at $x_0 = \psi(t_0)$ as

$$(3.11) \quad d_t^{\partial_t \psi} \hat{f}(t_0, x_0) := \left. \frac{d}{dt} \hat{f}(t, \psi(t)) \right|_{t=t_0}.$$

As a further consequence, the time derivative of \hat{f} at $x_0 = \mathbf{y}(t_0, \xi)$ along the parametrization $\mathbf{y}(\cdot, \xi)$ is defined analogously as

$$(3.12) \quad d_t^{\hat{\mathbf{V}}} \hat{f}(t_0, x_0) := \left. \frac{d}{dt} \hat{f}(t, \mathbf{y}(t, \xi)) \right|_{t=t_0}.$$

For a trajectory $\psi_{\hat{\mathbf{N}}}$ that passes through $x_0 \in \mathcal{M}_{t_0}$ at time t_0 and for which $\partial_t \psi_{\hat{\mathbf{N}}}(t_0)$ is orthogonal to $T_{x_0} \mathcal{M}_{t_0}$, the so-called *normal time derivative* of \hat{f} is defined as

$$(3.13) \quad d_t^{\hat{\mathbf{N}}} \hat{f}(t_0, x_0) := \left. \frac{d}{dt} \hat{f}(t, \psi_{\hat{\mathbf{N}}}(t)) \right|_{t=t_0}.$$

The relation between (3.11) and (3.13) is given by

$$(3.14) \quad d_t^{\partial_t \psi} \hat{f} = d_t^{\hat{\mathbf{N}}} \hat{f} + \nabla_{\mathcal{M}} \hat{f} \cdot \partial_t \psi.$$

See [12, sect. 3.3] for details. Figure 3 sketches the different trajectories and their velocities.

Recall that by assumption (3.7) we have $\hat{\mathbf{U}} = \partial_t \gamma$. With the help of definition (3.11) and relation (3.14) we can immediately recast assumption (3.10) and demand that along a trajectory γ , as defined in (3.4), we must have

$$(3.15) \quad d_t^{\hat{\mathbf{U}}} \hat{f} = d_t^{\hat{\mathbf{N}}} \hat{f} + \nabla_{\mathcal{M}} \hat{f} \cdot \hat{\mathbf{U}} \stackrel{!}{=} 0.$$

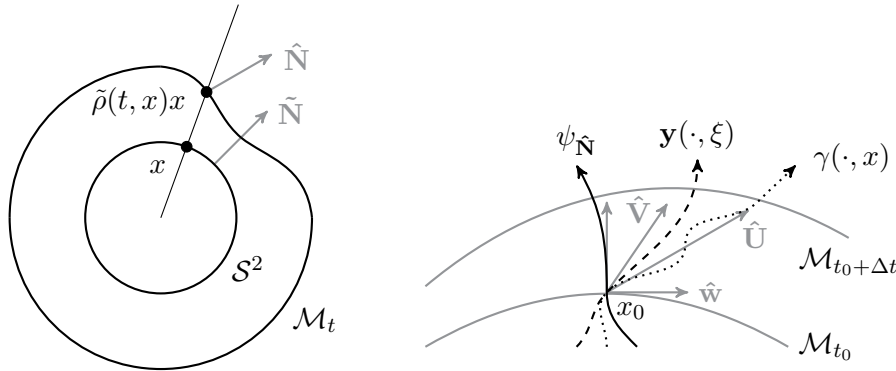


Figure 3. Left: Illustration of a cut through the surfaces S^2 and \mathcal{M}_t intersecting the origin. Surface normals are depicted in grey. Right: Sketch of various trajectories following the evolving surface. The corresponding velocities are depicted in grey. The velocity \hat{U} of a cell following γ is composed of the surface velocity \hat{V} and a tangential velocity \hat{w} .

However, this so-called *generalized optical flow equation* is inconvenient from a numerical perspective, as $d_t^{\hat{N}} \hat{f}$ typically is unknown or hard to estimate from real data. As a remedy, in [34, Lemma 2] proposes using

$$\begin{aligned} d_t^{\hat{N}} \hat{f} + \nabla_{\mathcal{M}} \hat{f} \cdot \hat{U} &\stackrel{(3.8)}{=} d_t^{\hat{N}} \hat{f} + \nabla_{\mathcal{M}} \hat{f} \cdot (\hat{V} + \hat{w}) \\ &\stackrel{(3.14)}{=} d_t^{\hat{V}} \hat{f} - \nabla_{\mathcal{M}} \hat{f} \cdot \hat{V} + \nabla_{\mathcal{M}} \hat{f} \cdot (\hat{V} + \hat{w}) \\ &= d_t^{\hat{V}} \hat{f} + \nabla_{\mathcal{M}} \hat{f} \cdot \hat{w}, \end{aligned}$$

which is a *parametrised optical flow equation*. We highlight that the unknown \hat{w} depends exclusively on the imposed surface velocity \hat{V} .

Computing the optical flow \hat{w} from data \hat{f} constitutes an ill-posed inverse problem because the above equation is underdetermined and a unique solution is not guaranteed. As a remedy, we minimize a Tikhonov-type functional consisting of a data term and a spatially varying regularization term. In what follows, we seek a minimizer to the functional $\mathcal{E} : H^1(\mathcal{M}_t, T\mathcal{M}_t) \rightarrow [0, +\infty]$,

$$(3.16) \quad \mathcal{E}(\hat{w}) := \|d_t^{\hat{V}} \hat{f} + \nabla_{\mathcal{M}} \hat{f} \cdot \hat{w}\|_{L^2(\mathcal{M}_t)}^2 + \mathcal{R}(\hat{w}),$$

where, given a measurable function $s(t, \cdot) : \mathcal{M}_t \rightarrow \{0, 1\}$, the regularization functional $\mathcal{R}(\hat{w})$ is defined as

$$(3.17) \quad \mathcal{R}(\hat{w}) := \alpha_0 \int_{\mathcal{M}_t} s \|\nabla \hat{w}\|_2^2 d\mathcal{M}_t + \alpha_1 \int_{\mathcal{M}_t} (1 - s) \|\hat{w}\|^2 d\mathcal{M}_t,$$

and $\alpha_0, \alpha_1 > 0$ are regularization parameters. Here, the function s incorporates a priori information about the support of the solution. The idea is that minimization of (3.16) with (3.17) as a regularization functional favors tangent vector fields of certain regularity in areas where data is present but, on the other hand, prevents potentially undesirable fill-in effects

of quadratic regularization in regions with no data. In practice one may choose s to be, e.g., a segmentation of the fluorescently labeled cells or, due to the nature of the fluorescence microscopy data, one may as well choose $s := \hat{f}$ with $\hat{f}(t, \cdot) : \mathcal{M}_t \rightarrow [0, 1]$. In this article, however, we restrict ourselves to functions $s(t, \cdot) : \mathcal{M}_t \rightarrow (0, 1)$ because, by the equivalence of norms, coercivity of \mathcal{E} with respect to $H^1(\mathcal{M}_t, T\mathcal{M}_t)$, and thus well-posedness of the problem, is guaranteed [8]. Moreover, let us emphasize that (3.16) is a generalization of [36], where only the Sobolev (semi)norm was used as a regularization functional.

3.2. Conservation of mass. Let us be given a time-evolving surface (3.1) which is migrating through a fluid defined in the ambient space. We stress that, in general, this surface is *nonmaterial*. In other words, the surface velocity $\hat{\mathbf{V}}$ induced by a chosen parametrization of \mathcal{M} is different from the fluid velocity $\hat{\mathbf{U}}$. Furthermore, let us denote by

$$\hat{f}(t, \cdot) : \mathcal{M}_t \rightarrow \mathbb{R}$$

the density of the fluid restricted to the surface \mathcal{M}_t . With the goal of estimating the fluid motion, we assume that this data \hat{f} satisfies mass preservation.

In order to derive a suitable conservation law, let us consider an arbitrary evolving subsurface $\Gamma_t \subseteq \mathcal{M}_t$ of this surface. For the sake of simplicity we will omit the index and write Γ (respectively, $\partial\Gamma$) for the subsurface and its boundary.

The boundary curve $\partial\Gamma$ is oriented by its exterior unit normal field $\hat{\nu}$. Recall that $\hat{\nu}$ is normal to $\partial\Gamma$ and tangent to \mathcal{M}_t . We denote by $\hat{\mathbf{V}}_{\partial\Gamma} \in \mathbb{R}^3$ the velocity of the curve $\partial\Gamma$ as it moves through the embedding space. Its intrinsic component, which is independent of the parametrization of the curve $\partial\Gamma$, is denoted by

$$V_{\partial\Gamma} := \hat{\mathbf{V}}_{\partial\Gamma} \cdot \hat{\nu}.$$

Since by assumption we have that $\Gamma \subseteq \mathcal{M}_t$, we deduce that

$$\hat{\mathbf{V}}_{\partial\Gamma} \cdot \hat{\mathbf{N}} = V.$$

In other words, Γ and \mathcal{M}_t evolve with equal normal velocities. Furthermore, the *normal migrational velocity* $V_{\partial\Gamma}^{\text{mig}}$ of the curve $\partial\Gamma$, as it travels through the fluid, is defined by

$$V_{\partial\Gamma}^{\text{mig}} := (\hat{\mathbf{V}}_{\partial\Gamma} - \hat{\mathbf{U}}) \cdot \hat{\nu}.$$

Given a fluid density \hat{f} and an arbitrary evolving subsurface $\Gamma \subseteq \mathcal{M}_t$, the transport relation

$$(3.18) \quad \frac{d}{dt} \int_{\Gamma} \hat{f} \, d\Gamma = \int_{\Gamma} \left(d_t^{\hat{\mathbf{N}}} \hat{f} + \nabla_{\mathcal{M}} \cdot (\hat{f} \hat{\mathbf{u}}) - \hat{f} K V \right) d\Gamma + \int_{\partial\Gamma} \hat{f} V_{\partial\Gamma}^{\text{mig}} \, d\Gamma$$

holds. We refer the reader to [12, sect. 4.2] for details. Here, $\hat{\mathbf{u}}$ is the tangent part (3.9) of the fluid velocity, $\nabla_{\mathcal{M}} \cdot (\hat{f} \hat{\mathbf{u}})$ denotes the divergence of $\hat{f} \hat{\mathbf{u}}$, and K is the total curvature.

Recall that at the beginning of this section we assumed that the surface \mathcal{M}_t evolves with (scalar) normal velocity $V = \hat{\mathbf{U}} \cdot \hat{\mathbf{N}}$; see (3.7). In addition, let us suppose that Γ is *material*,

meaning that it convects with the fluid. In other words, it holds that

$$\hat{\mathbf{V}}_{\partial\Gamma} = \hat{\mathbf{U}}.$$

As a consequence, we have $V_{\partial\Gamma}^{\text{mig}} = 0$, and the transport relation (3.18) simplifies to

$$\frac{d}{dt} \int_{\Gamma} \hat{f} \, d\Gamma = \int_{\Gamma} \left(d_t^{\hat{\mathbf{N}}} \hat{f} + \nabla_{\mathcal{M}} \cdot (\hat{f} \hat{\mathbf{u}}) - \hat{f} KV \right) d\Gamma.$$

Since Γ is material, conservation of mass requires that

$$\frac{d}{dt} \int_{\Gamma} \hat{f} \, d\Gamma \stackrel{!}{=} 0,$$

and we obtain the relation

$$\int_{\Gamma} \left(d_t^{\hat{\mathbf{N}}} \hat{f} + \nabla_{\mathcal{M}} \cdot (\hat{f} \hat{\mathbf{u}}) - \hat{f} KV \right) d\Gamma = 0.$$

Since Γ was arbitrary, this leads to the pointwise conservation law

$$(3.19) \quad d_t^{\hat{\mathbf{N}}} \hat{f} + \nabla_{\mathcal{M}} \cdot (\hat{f} \hat{\mathbf{u}}) - \hat{f} KV = 0,$$

which, following the terminology from before, resembles a *generalized continuity equation*. As for the generalized optical flow equation, we utilize relation (3.14) with time derivative (3.12) and obtain a parametrized mass preservation constraint

$$(3.20) \quad d_t^{\hat{\mathbf{V}}} \hat{f} + \nabla_{\mathcal{M}} \cdot (\hat{f} \hat{\mathbf{u}}) - \hat{f} KV - \nabla_{\mathcal{M}} \hat{f} \cdot \hat{\mathbf{v}} = 0,$$

where $\hat{\mathbf{v}}$ is the tangent part of the surface velocity (3.3). We refer to it as the *parametrized continuity equation*.

Again, let $t \in I$ be fixed. In view of the ill-posedness of (3.20), we seek a minimizer to the functional $\mathcal{F} : H^1(\mathcal{M}_t, T\mathcal{M}_t) \rightarrow [0, +\infty]$,

$$(3.21) \quad \mathcal{F}(\hat{\mathbf{u}}) := \|d_t^{\hat{\mathbf{N}}} \hat{f} + \nabla_{\mathcal{M}} \cdot (\hat{f} \hat{\mathbf{u}}) - \hat{f} KV\|_{L^2(\mathcal{M}_t)}^2 + \mathcal{R}(\hat{\mathbf{u}}) + \mathcal{S}(\hat{\mathbf{u}}),$$

where $\mathcal{R}(\hat{\mathbf{u}})$ is defined as in (3.17) and

$$(3.22) \quad \mathcal{S}(\hat{\mathbf{u}}) := \alpha_2 \int_{\mathcal{M}_t} (1-s)(\nabla_{\mathcal{M}} \cdot \hat{\mathbf{u}})^2 \, d\mathcal{M}_t.$$

Here, $\alpha_2 > 0$ is a regularization parameter. The main reason for this additional term in comparison to (3.16) is to ensure the well-definedness of the data term in (3.21). Moreover, in the presence of noise it helps to reduce oscillations; see section 5.

3.3. Discussion. The main differences between the two models are as follows. First, they differ in the assumptions on \hat{f} . While conservation of brightness requires the image intensities to stay constant along characteristics, conservation of mass allows them to change and is therefore more general. Deciding which model to choose depends on the specific application and on available a priori information about the considered data. Second, in (3.16) the unknown is $\hat{\mathbf{w}}$, whereas in (3.21) the unknown is $\hat{\mathbf{u}}$. As a result, the latter allows us to estimate the entire tangential part of the unknown (cell) velocity $\hat{\mathbf{U}}$, whereas the former only yields a tangent vector field that is relative to the prescribed—and in practice often unknown—surface velocity. In practical applications this difference could be crucial because one needs to potentially care less about the chosen parametrization. Third, as we employ a variational approach, the models differ in their regularity assumptions. The first approach enforces regularity of $\hat{\mathbf{w}}$, whereas the second enforces regularity $\hat{\mathbf{u}}$. The main disadvantage of using (3.21) is that it requires evaluation of additional quantities, such as the divergence of the unknown, the total curvature, and the normal velocity. Let us also mention that, in order to derive (3.19), we required the additional assumption of arbitrary subsurfaces being material.

4. Numerical solution. In this section, we propose a mesh-free Galerkin method based on compactly supported (tangent) vectorial basis functions.

4.1. Spherical basis functions. Let $h \in (0, 1)$ and let $k \in \mathbb{N}_0 = \{0, 1, 2, \dots\}$. We define the 1-dimensional piecewise polynomial function $b_h^{(k)} : [-1, 1] \rightarrow \mathbb{R}$ as

$$b_h^{(k)}(\tau) = \begin{cases} 0 & \text{for } -1 \leq \tau \leq h, \\ \frac{(\tau-h)^k}{(1-h)^k} & \text{for } h < \tau \leq 1. \end{cases}$$

The parameter h controls the support, and k is its degree. For a point $x_j \in \mathcal{S}^2$ we define the x_j -zonal function

$$(4.1) \quad \tilde{b}_j : \mathcal{S}^2 \rightarrow \mathbb{R}, \quad x \mapsto b_h^{(k)}(x_j \cdot x),$$

which is compactly supported on \mathcal{S}^2 ; see [20, 49]. Moreover, we define the tangent vector fields

$$(4.2) \quad \begin{aligned} \tilde{\mathbf{y}}_j^{(1)} &:= \nabla_{\mathcal{S}^2} \tilde{b}_j, \\ \tilde{\mathbf{y}}_j^{(2)} &:= \nabla_{\mathcal{S}^2} \tilde{b}_j \times \tilde{\mathbf{N}}, \end{aligned}$$

where $\tilde{\mathbf{N}}$ is the outward unit normal of \mathcal{S}^2 . See Figure 4 for an illustration.

4.2. Finite-dimensional approximation. The chosen parametrization \mathbf{y} in (2.1) naturally admits a smooth map $\tilde{\phi}(t, \cdot) : \mathcal{S}^2 \rightarrow \mathcal{M}_t$ of the form

$$\tilde{\phi}(t, x) : x \mapsto \tilde{\rho}(t, x)x.$$

By the product rule, the differential $D\tilde{\phi}(t, x) : T_x \mathcal{S}^2 \rightarrow T_{\tilde{\phi}(t, x)} \mathcal{M}_t$ of $\tilde{\phi}$ is given by

$$D\tilde{\phi}(t, x) = \tilde{\rho}(t, x)\text{Id} + x\nabla_{\mathcal{S}^2} \tilde{\rho}(t, x)^\top \in \mathbb{R}^{3 \times 3}.$$

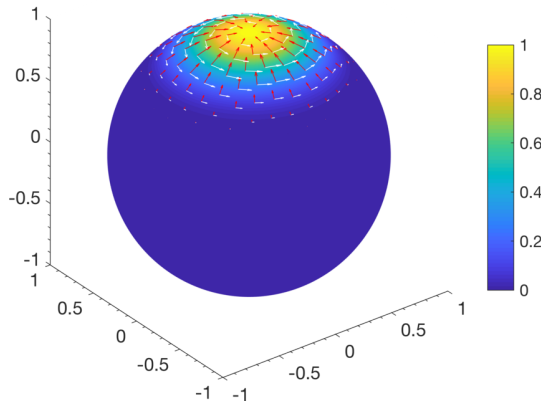


Figure 4. Vectorial basis functions $\tilde{\mathbf{y}}_j^{(1)}$ (red) and $\tilde{\mathbf{y}}_j^{(2)}$ (white) and the corresponding zonal function \tilde{b}_j centered at the north pole $x_j = (0, 0, 1)^\top$. The parameters of the corresponding function $b_h^{(k)}$ were chosen as $k = 3$ and $h = 0.6$.

Let us be given a set $\{x_j \in \mathcal{S}^2\}_{j=1,\dots,N}$ of pairwise distinct points on the 2-sphere. With each of its elements x_j we associate the x_j -zonal function \tilde{b}_j ; see (4.1). According to definition (4.2), we immediately obtain the set

$$(4.3) \quad \left\{ \tilde{\mathbf{y}}_j^{(i)} : j = 1, \dots, N, i = 1, 2 \right\}$$

of tangent vector fields on \mathcal{S}^2 . We approximate the solutions to the problems

$$\min_{\hat{\mathbf{w}} \in H^1(\mathcal{M}_t, T\mathcal{M}_t)} \mathcal{E}(\hat{\mathbf{w}}) \quad \text{and} \quad \min_{\hat{\mathbf{u}} \in H^1(\mathcal{M}_t, T\mathcal{M}_t)} \mathcal{F}(\hat{\mathbf{u}})$$

in a finite-dimensional subspace $\mathcal{U} \subset H^1(\mathcal{M}_t, T\mathcal{M}_t)$, where \mathcal{E} and \mathcal{F} are defined as in (3.16) and (3.21), respectively. We define this space of tangent vector fields on \mathcal{M}_t as

$$(4.4) \quad \mathcal{U} := \text{span} \left\{ \hat{\mathbf{y}}_j^{(i)} : j = 1, \dots, N, i = 1, 2 \right\},$$

where $\hat{\mathbf{y}}_j^{(i)} = D\tilde{\phi}(t, \cdot)(\tilde{\mathbf{y}}_j^{(i)})$ is the pushforward of an element $\tilde{\mathbf{y}}_j^{(i)}$ contained in the set (4.3) by means of the differential $D\tilde{\phi}$. For notational convenience, we relabel the elements of \mathcal{U} with the help of an index set $J_{\mathcal{U}} \subset \mathbb{N}$ and use a single index letter $p \in J_{\mathcal{U}}$.

In the following, we derive optimality conditions for minimizers of the functionals (3.16) and (3.21).

4.3. Conservation of brightness. We expand the sought-after tangent vector field as

$$(4.5) \quad \hat{\mathbf{w}} = \sum_{p \in J_{\mathcal{U}}} w_p \hat{\mathbf{y}}_p,$$

where $w_p \in \mathbb{R}$, $p \in J_{\mathcal{U}}$, are the unknown coefficients. By plugging ansatz (4.5) into functional (3.16), for the data term we obtain

$$\int_{\mathcal{M}_t} \left(d_t \hat{\mathbf{V}} \hat{f} + \sum_{p \in J_{\mathcal{U}}} w_p (\nabla_{\mathcal{M}} \hat{f} \cdot \hat{\mathbf{y}}_p) \right)^2 d\mathcal{M}_t.$$

In order to compute the regularization functional $\mathcal{R}(\hat{\mathbf{w}})$ in (3.17), we require an expression for the Hilbert–Schmidt norm of the covariant derivative of $\hat{\mathbf{w}}$. For an element $\partial_i \mathbf{y}$ of the coordinate basis and $\hat{\mathbf{v}} = v^j \partial_j \mathbf{y}$, the covariant derivative reads

$$\nabla_{\partial_i \mathbf{y}} \hat{\mathbf{v}} = (\partial_i v^j + v^k \Gamma_{ik}^j) \partial_j \mathbf{y};$$

see [37, Lemma 4.3]. Here, Γ_{ik}^j denote the Christoffel symbols with regard to the coordinate basis, that is, $\nabla_{\partial_i \mathbf{y}} \partial_k \mathbf{y} = \Gamma_{ik}^j \partial_j \mathbf{y}$. Let us denote the above coefficients by

$$(4.6) \quad D_i v^j := \partial_i v^j + v^k \Gamma_{ik}^j.$$

Then for $\hat{\mathbf{y}}_p = y_p^k \partial_k \mathbf{y}$ we find, with the help of Lemma A.1 and the fact that (4.6) is linear, that

$$\|\nabla \sum_{p \in J_{\mathcal{U}}} w_p \hat{\mathbf{y}}_p\|_2^2 = \sum_{p, q \in J_{\mathcal{U}}} w_p w_q g_{k\ell} g^{ij} D_i y_p^k D_j y_q^\ell,$$

where $g_{k\ell}$ and g^{ij} are the components of the metric (2.5) and of its inverse, respectively. Moreover, for the second term in (3.17) we obtain

$$\|\sum_{p \in J_{\mathcal{U}}} w_p \hat{\mathbf{y}}_p\|^2 = \sum_{p, q \in J_{\mathcal{U}}} w_p w_q (\hat{\mathbf{y}}_p \cdot \hat{\mathbf{y}}_q).$$

The optimality conditions for $\mathcal{E}(\hat{\mathbf{w}})$ are obtained by taking $\partial \mathcal{E} / \partial w_p = 0$ for all $p \in J_{\mathcal{U}}$ and in matrix-vector form read

$$(4.7) \quad (A + \alpha_0 C + \alpha_1 D) w = b,$$

where $w = (w_1, \dots, w_{|J_{\mathcal{U}}|})^\top \in \mathbb{R}^{|J_{\mathcal{U}}|}$ denotes the vector of unknowns. The entries of the matrix $A = (a_{pq})$ corresponding to the data term are given by

$$a_{pq} = \int_{\mathcal{M}_t} (\nabla_{\mathcal{M}} \hat{f} \cdot \hat{\mathbf{y}}_p) (\nabla_{\mathcal{M}} \hat{f} \cdot \hat{\mathbf{y}}_q) d\mathcal{M}_t,$$

whereas the entries of the matrices $C = (c_{pq})$ and $D = (d_{pq})$ corresponding to the regularization terms are given by

$$c_{pq} = \int_{\mathcal{M}_t} s g_{k\ell} g^{ij} D_i y_p^k D_j y_q^\ell d\mathcal{M}_t$$

and

$$d_{pq} = \int_{\mathcal{M}_t} (1-s)(\hat{\mathbf{y}}_p \cdot \hat{\mathbf{y}}_q) d\mathcal{M}_t,$$

respectively. The entries of the vector $b = (b_p)$ are

$$b_p = - \int_{\mathcal{M}_t} d_t^{\hat{\mathbf{V}}} \hat{f} (\nabla_{\mathcal{M}} \hat{f} \cdot \hat{\mathbf{y}}_p) d\mathcal{M}_t.$$

4.4. Conservation of mass. Next, let us derive the optimality conditions for the functional \mathcal{F} defined in (3.21). For numerical convenience we use (3.20) rather than (3.19) as they are equivalent. Accordingly, we expand the sought-after tangent vector field as

$$\hat{\mathbf{u}} = \sum_{p \in J_{\mathcal{U}}} u_p \hat{\mathbf{y}}_p,$$

where $u_p \in \mathbb{R}$, $p \in J_{\mathcal{U}}$, are the unknown coefficients. For the data term we get

$$\int_{\mathcal{M}_t} \left(d_t^{\hat{\mathbf{V}}} \hat{f} + \sum_{p \in J_{\mathcal{U}}} u_p (\nabla_{\mathcal{M}} \hat{f} \cdot \hat{\mathbf{y}}_p + \hat{f} \nabla_{\mathcal{M}} \cdot \hat{\mathbf{y}}_p) - \hat{f} KV - \nabla_{\mathcal{M}} \hat{f} \cdot \hat{\mathbf{v}} \right)^2 d\mathcal{M}_t.$$

Regarding the term $\mathcal{S}(\hat{\mathbf{u}})$ in the functional (3.21), we find that

$$\left(\nabla_{\mathcal{M}} \cdot \sum_{p \in J_{\mathcal{U}}} u_p \hat{\mathbf{y}}_p \right)^2 = \sum_{p, q \in J_{\mathcal{U}}} u_p u_q (\nabla_{\mathcal{M}} \cdot \hat{\mathbf{y}}_p) (\nabla_{\mathcal{M}} \cdot \hat{\mathbf{y}}_q).$$

Analogously to before, by taking $\partial \mathcal{F} / \partial u_p = 0$ for all $p \in J_{\mathcal{U}}$, we obtain the optimality conditions in matrix-vector form

$$(4.8) \quad (A + \alpha_0 C + \alpha_1 D + \alpha_2 E)u = b,$$

where the matrices C and D are as before. The entries of the matrix $A = (a_{pq})$ corresponding to the data term are

$$a_{pq} = \int_{\mathcal{M}_t} (\nabla_{\mathcal{M}} \hat{f} \cdot \hat{\mathbf{y}}_p + \hat{f} \nabla_{\mathcal{M}} \cdot \hat{\mathbf{y}}_p) (\nabla_{\mathcal{M}} \hat{f} \cdot \hat{\mathbf{y}}_q + \hat{f} \nabla_{\mathcal{M}} \cdot \hat{\mathbf{y}}_q) d\mathcal{M}_t.$$

The entries of the matrix $E = (e_{pq})$ corresponding to the regularization term (3.22) are given by

$$e_{pq} = \int_{\mathcal{M}_t} (1-s) (\nabla_{\mathcal{M}} \cdot \hat{\mathbf{y}}_p) (\nabla_{\mathcal{M}} \cdot \hat{\mathbf{y}}_q) d\mathcal{M}_t.$$

Finally, the vector $b = (b_p)$ now reads

$$b_p = - \int_{\mathcal{M}_t} (d_t^{\hat{\mathbf{V}}} \hat{f} - \hat{f} KV - \nabla_{\mathcal{M}} \hat{f} \cdot \hat{\mathbf{v}}) (\nabla_{\mathcal{M}} \hat{f} \cdot \hat{\mathbf{y}}_p) d\mathcal{M}_t.$$

4.5. Surface parametrization. The main goal of this subsection is to estimate the time-evolving surface \mathcal{M} together with a parametrization \mathbf{y} of the form (2.1). We extend the idea of surface interpolation from scattered data in [36]. Given noisy data $\tilde{\rho}^\delta : I \times \mathcal{S}^2 \rightarrow (0, \infty)$, we seek a minimizer $\tilde{\rho} : I \times \mathcal{S}^2 \rightarrow (0, \infty)$ to the energy

$$(4.9) \quad \mathcal{G}(\tilde{\rho}) := \int_I \left(\|\tilde{\rho}(t, \cdot) - \tilde{\rho}^\delta(t, \cdot)\|_{L^2(\mathcal{S}^2)}^2 + \beta_0 |\tilde{\rho}(t, \cdot)|_{H^r(\mathcal{S}^2)}^2 + \beta_1 \|\partial_t \tilde{\rho}(t, \cdot)\|_{L^2(\mathcal{S}^2)}^2 \right) dt.$$

Here, $\beta_0, \beta_1 > 0$ are regularization parameters balancing the terms, and $|\cdot|_{H^r(\mathcal{S}^2)}$ is the Sobolev seminorm on \mathcal{S}^2 of order $r > 0$. While the above problem is stated in an infinite-dimensional setting, only finitely many (point) evaluations are available in practice. For each frame $t \in \{0, \dots, T\}$, we are given $N_t \geq 0$ noisy measurements $\{\tilde{\rho}^\delta(t, x_i) : x_i \in \mathcal{S}^2\}_{i=1}^{N_t}$ at pairwise distinct points on \mathcal{S}^2 . Approximate locations of cell centers serve as measurements, cf. section 5.2. Due to the form (2.1), the values of the point evaluations are given by

$$(4.10) \quad \tilde{\rho}^\delta(t, \bar{x}_i) = \|x_i\|, \quad x_i \in \mathbb{R}^3 \setminus \{0\}, \quad t \in \{0, \dots, T\}, \quad i \in \{1, \dots, N_t\},$$

where $\bar{x}_i = x_i/\|x_i\|$ is the radial projection onto the 2-sphere. In total, at least one sample point is required. In order to minimize (4.9) approximately, we consider projections of $\tilde{\rho}$ onto a finite-dimensional subspace spanned by (scalar) spherical harmonics, as they can be conveniently related to the regularization functionals in (4.9).

For $n \in \mathbb{N}_0$, an element $\tilde{Y}_n \in \text{Harm}_n$ of the space of harmonic polynomials in \mathbb{R}^3 that are of degree n and are restricted to \mathcal{S}^2 is referred to as a *spherical harmonic*. It is an infinitely often differentiable eigenfunction of the Laplace–Beltrami operator $\Delta_{\mathcal{S}^2}$ on \mathcal{S}^2 , and its corresponding eigenvalue is $\lambda_n = n(n+1)$. Moreover, $\dim(\text{Harm}_n) = 2n+1$. See Lemma 5.8 and Theorem 5.6 in [42].

The set $\{\tilde{Y}_{n,j} : n \in \mathbb{N}_0, j = 1, \dots, 2n+1\}$ is a complete orthonormal system in $L^2(\mathcal{S}^2)$ with respect to $\langle \cdot, \cdot \rangle_{L^2(\mathcal{S}^2)}$. As a consequence, the sought-after function $\tilde{\rho}(t, \cdot) \in L^2(\mathcal{S}^2)$ can be uniquely expanded in its Fourier series representation as

$$\tilde{\rho}(t, \cdot) = \sum_{n=0}^{\infty} \sum_{j=1}^{2n+1} \langle \tilde{\rho}(t, \cdot), \tilde{Y}_{n,j} \rangle_{L^2(\mathcal{S}^2)} \tilde{Y}_{n,j};$$

see Theorem 5.25 in [42]. We assume that $\tilde{Y}_{n,j} \in \text{Harm}_n$ are *fully normalized spherical harmonics* [42, sect. 5.2]. By Parseval’s identity, we furthermore have

$$\|\tilde{\rho}(t, \cdot)\|_{L^2(\mathcal{S}^2)}^2 = \sum_{n,j} \langle \tilde{\rho}(t, \cdot), \tilde{Y}_{n,j} \rangle_{L^2(\mathcal{S}^2)}^2.$$

Again, see Theorem 5.25 in [42]. As a further consequence, the Sobolev space $H^r(\mathcal{S}^2)$ can be defined for arbitrary $r \in \mathbb{R}$ by means of the completion of all $C^\infty(\mathcal{S}^2)$ functions with respect to the norm

$$\|\tilde{\rho}(t, \cdot)\|_{H^r(\mathcal{S}^2)}^2 := \|(\Delta_{\mathcal{S}^2} + 1)^{r/2} \tilde{\rho}(t, \cdot)\|_{L^2(\mathcal{S}^2)}^2 = \sum_{n,j} (\lambda_n + 1)^r \langle \tilde{\rho}(t, \cdot), \tilde{Y}_{n,j} \rangle_{L^2(\mathcal{S}^2)}^2.$$

For $r \in \mathbb{R}$, the $H^r(\mathcal{S}^2)$ seminorm of order r in (4.9) is defined as

$$(4.11) \quad |\tilde{\rho}(t, \cdot)|_{H^r(\mathcal{S}^2)}^2 := \|\Delta_{\mathcal{S}^2}^{r/2} \tilde{\rho}(t, \cdot)\|_{L^2(\mathcal{S}^2)}^2 = \sum_{n,j} \lambda_n^r \langle \tilde{\rho}(t, \cdot), \tilde{Y}_{n,j} \rangle_{L^2(\mathcal{S}^2)}^2.$$

We approximate the solution to $\min_{\tilde{\rho}} \mathcal{G}(\tilde{\rho})$ in a finite-dimensional subspace $\mathcal{Q} \subset H^r(\mathcal{S}^2)$, chosen as $\mathcal{Q} := \text{span}\{\tilde{Y}_p : p \in J_{\mathcal{Q}}\}$, where $J_{\mathcal{Q}} \subset \mathbb{N}$ again is an index set and \tilde{Y}_p are the fully normalized scalar spherical harmonics defined above. For a time instant $t \in \{0, \dots, T\}$, the sought-after function is thus expanded as

$$(4.12) \quad \tilde{\rho}(t, \cdot) = \sum_{p \in J_{\mathcal{Q}}} \varrho_p(t) \tilde{Y}_p,$$

where $\varrho_p(t) \in \mathbb{R}$, for $p \in J_{\mathcal{Q}}$, are the time-dependent, unknown coefficients. From (4.12) we find that

$$\partial_t \tilde{\rho}(t, \cdot) = \partial_t \sum_{p \in J_{\mathcal{Q}}} \varrho_p(t) \tilde{Y}_p = \sum_{p \in J_{\mathcal{Q}}} \partial_t \varrho_p(t) \tilde{Y}_p.$$

Thus, for the last term in (4.9) we have

$$\begin{aligned} \|\partial_t \tilde{\rho}(t, \cdot)\|_{L^2(\mathcal{S}^2)}^2 &= \left\| \sum_{p \in J_{\mathcal{Q}}} \partial_t \varrho_p(t) \tilde{Y}_p \right\|_{L^2(\mathcal{S}^2)}^2 \\ &= \int_{\mathcal{S}^2} \left(\sum_{p \in J_{\mathcal{Q}}} \partial_t \varrho_p(t) \tilde{Y}_p \right)^2 d\mathcal{S}^2 \\ &= \int_{\mathcal{S}^2} \sum_{p \in J_{\mathcal{Q}}} \sum_{q \in J_{\mathcal{Q}}} \partial_t \varrho_p(t) \partial_t \varrho_q(t) \tilde{Y}_p \tilde{Y}_q d\mathcal{S}^2 \\ &= \sum_{p \in J_{\mathcal{Q}}} \sum_{q \in J_{\mathcal{Q}}} \partial_t \varrho_p(t) \partial_t \varrho_q(t) \int_{\mathcal{S}^2} \tilde{Y}_p \tilde{Y}_q d\mathcal{S}^2 \\ &= \sum_{p \in J_{\mathcal{Q}}} (\partial_t \varrho_p(t))^2, \end{aligned}$$

where the last identity follows from the orthogonality of spherical harmonics. We approximate the partial derivatives with respect to time with the backward difference $\partial_t \varrho_p(t) \approx \varrho_p(t) - \varrho_p(t - 1)$. By plugging (4.12) into (4.9), utilizing definition (4.11), and taking $\partial \mathcal{G} / \partial \varrho_p(t)$ for all $p \in J_{\mathcal{Q}}$ and all $t \in \{0, \dots, T\}$, we obtain the linear system of optimality conditions

$$(4.13) \quad \begin{aligned} \sum_{q \in J_{\mathcal{Q}}} \varrho_q(t) \left(\sum_{i=1}^{N_t} \tilde{Y}_p(\bar{x}_i) \tilde{Y}_q(\bar{x}_i) \right) + (\beta_0 \lambda_p^r + 2\beta_1) \varrho_p(t) \\ - \beta_1 \varrho_p(t - 1) - \beta_1 \varrho_p(t + 1) = \sum_{i=1}^{N_t} \|x_i\| \tilde{Y}_p(\bar{x}_i), \quad p \in J_{\mathcal{Q}}, \end{aligned}$$

and enforce (temporal) zero Neumann boundary conditions at $t = 0$ and $t = T$.

4.6. Evaluation of integrals. In order to solve the linear systems (4.7) and (4.8), it remains to discuss the numerical evaluation of the integrals and the construction of the set (4.3) of basis functions. For each time instant $t \in I$, we rewrite the integrals in terms of integrals on the 2-sphere and apply a suitable cubature rule.

Given M evaluation points $x_i \in \mathcal{S}^2$ and corresponding weights $q_i \in \mathbb{R}$, we approximate the surface integral of a function $\hat{f} : \mathcal{M}_t \rightarrow \mathbb{R}$ by

$$\int_{\mathcal{M}_t} \hat{f} d\mathcal{M}_t = \int_{\mathcal{S}^2} \tilde{f} \tilde{\rho} \sqrt{\|\nabla_{\mathcal{S}^2} \tilde{\rho}\|^2 + \tilde{\rho}^2} d\mathcal{S}^2 \approx \sum_{i=1}^M (\tilde{f} \tilde{\rho} \sqrt{\|\nabla_{\mathcal{S}^2} \tilde{\rho}\|^2 + \tilde{\rho}^2})(x_i) q_i,$$

where $\tilde{f} : \mathcal{S}^2 \rightarrow \mathbb{R}$ is defined in (2.2) and the first identity is proved in [36, Lemma 2.1].

Since our data is supported only on the upper hemisphere (see sect. 5.1), we assume that the coefficients of vectorial basis functions centered at $x_j^3 < 0$ are zero. As a result, the number of unknowns in the linear systems (4.7) and (4.8) is halved. Moreover, we choose a cubature rule for integration over the spherical cap

$$\mathcal{C} := \{x \in \mathcal{S}^2 : \arccos(x \cdot \mathbf{e}_3) \leq \pi/2\} \subset \mathcal{S}^2,$$

where $\mathbf{e}_3 = (0, 0, 1)^\top \in \mathbb{R}^3$ is the unit vector pointing in the x^3 -direction; see [24, sect. 7.1].

To achieve an approximately uniform placement of basis functions (4.3) on the upper hemisphere, we generate a polyhedral approximation $\mathcal{S}_h^2 = (\mathcal{V}, \mathcal{T})$ of \mathcal{S}^2 . Here, $\mathcal{V} = \{v_1, \dots, v_n\} \subset \mathcal{S}^2$ is the set of vertices and \mathcal{T} the set of triangular faces. This triangular mesh is generated by iterative refinement of an icosahedron which is inscribed in the sphere [11, Chapter 1.3.3]. In every refinement step the edge lengths are halved by connecting the edge midpoints and projecting them onto the unit sphere. The number of vertices of \mathcal{S}_h^2 in iteration $\ell \in \mathbb{N}_0$ is $n = 2 + 10 \cdot 4^\ell$. For the placement of basis functions (4.3) we choose $\mathcal{V} \cap \mathcal{C}$ as center points, resulting in approximately n basis functions, as every point in this set gives rise to two basis functions; cf. (4.2).

5. Experiments.

5.1. Microscopy data. The data at hand is volumetric time-lapse (4-dimensional) images of a living zebrafish embryo. The images were recorded with confocal laser-scanning microscopy during the gastrula period of the animal, taking place approximately five to ten hours after its fertilization. The sequence features endodermal cells labeled with a green fluorescence protein, and therefore they can be observed separately from the background. We refer the reader to [40] for information on the imaging techniques and to [43] for the treatment of the specimen.

The microscopy data contains a cuboid region of approximately $860 \times 860 \times 320 \mu\text{m}^3$ at a spatial resolution of $512 \times 512 \times 44$ voxels. Due to limitations of the microscopy technique, it contains only approximately half of the spherical-shaped embryo and exhibits noise contamination. Before data acquisition, the embryo was rotated so that the animal pole points upward and is contained in the cuboid region. Image intensities are in the range of $\{0, \dots, 255\}$. A representative sequence contains 151 frames recorded at an interval of 120 s. We denote the recorded data by $f^\delta \in \{0, \dots, 255\}^{151 \times 512 \times 512 \times 44}$. See Figure 1 for the unprocessed data.

5.2. Preprocessing and surface data acquisition. In this section, we briefly outline how we extract an image sequence \hat{f} together with the time-evolving sphere-like surface \mathcal{M} from said microscopy data. We use the approximate centers of cell nuclei as sample points of the surface. They represent local maxima in image intensity and can be found with sufficient accuracy by using Gaussian filtering in each frame $f^\delta(t, \cdot)$ followed by thresholding. However, before we solve the surface interpolation problem (4.9), the points are centered around the origin by fitting one single sphere to the union of all thresholded local maxima and subsequently subtracting the spherical center. Then measurements (4.10) are computed, and the system (4.13) of optimality conditions is solved. Then all surface quantities can be computed.

It remains to discuss the numerical approximation of the image sequence \hat{f} , its partial derivative $\partial_t \hat{f}$, and the gradient $\nabla_{\mathcal{M}} \hat{f}$. For each frame $t \in \{0, \dots, T\}$, we obtain surface data $\hat{f}(t, x)$ at $x \in \mathcal{M}_t$ via the radial projection

$$(5.1) \quad \hat{f}(t, x) := \max_{c \in [1-\varepsilon, 1+\varepsilon]} \hat{f}^\delta(t, cx),$$

where $\varepsilon > 0$ is chosen sufficiently large. By \hat{f}^δ we denote the piecewise linear extension of f^δ to \mathbb{R}^3 , which is required for gridded data. Before we do so, the intensities f^δ are scaled to the interval $[0, 1]$. The above projection (5.1) selects the maximum fluorescence-intensity within a narrow band around \mathcal{M}_t and thereby allows for small deviations of the cell nuclei from the fitted surface. See Figures 6 and 7 for illustrations.

Furthermore, we approximate the surface gradient of \hat{f} as

$$(5.2) \quad \nabla_{\mathcal{M}} \hat{f}(t, x) := P_{\mathcal{M}}(t, x) \left[\operatorname{mean}_{c \in [1-\varepsilon, 1+\varepsilon]} \nabla_{\mathbb{R}^3} \hat{f}^\delta(t, cx) \right],$$

where $P_{\mathcal{M}}$ is the orthogonal projector defined in (2.4). Here, $\nabla_{\mathbb{R}^3} \hat{f}^\delta$ is approximated by central differences inside the cuboid and by one-sided differences at the boundaries. We stress that in the above projection the parameter ε must be chosen with care as zero values influence the magnitude of the projection (5.2) and, as a further consequence, of the estimated velocity fields.

Finally, for $t = \{0, \dots, T-1\}$, the partial derivative of \hat{f} with respect to time is approximated by the forward difference $\partial_t \hat{f}(t, \cdot) \approx \hat{f}(t+1, \cdot) - \hat{f}(t, \cdot)$.

5.3. Visualization of results. We utilize the standard flow color-coding for the visualization of vector fields [6]. The idea is to create a color image representation of a (planar) vector field by assigning each vector a color and an intensity value from a predefined color disk. The color and the intensity associated with a vector are determined by its angle (respectively, its length). Typically, the radius R of the color disk is chosen to be equal to the length of the longest vector in the vector field one attempts to visualize.

In [34, 36], the idea has been extended to illustrate vector fields on surfaces. However, before assigning a color and an intensity to a—not necessarily tangent—vector, it is projected to the plane and then scaled to its original length, provided that the length of the projection is nonzero. Let us denote by $P_{x^3} : (x^1, x^2, x^3)^\top \rightarrow (x^1, x^2, 0)^\top$ the orthogonal projector of \mathbb{R}^3 onto the x^1 - x^2 -plane. Then for a general surface vector field $\hat{\mathbf{X}}(t, \cdot) : \mathcal{M}_t \rightarrow \mathbb{R}^3$, we apply the

color-coding to the scaled projection,

$$\hat{\mathbf{X}} \mapsto \begin{cases} \frac{\|\hat{\mathbf{X}}\|}{\|P_{x^3}\hat{\mathbf{X}}\|} P_{x^3}\hat{\mathbf{X}} & \text{if } \|P_{x^3}\hat{\mathbf{X}}\| > 0, \\ 0 & \text{else,} \end{cases}$$

and map the resulting color image back onto the surface. As a result, the lengths of the individual vectors are preserved, provided that they do not vanish in the projection. We assume that each \mathcal{M}_t is such that P_{x^3} is injective.

In order to evaluate the computed velocity fields, we create another triangular mesh $\mathcal{S}_{h'}$ similar to the one in section 4.6. Vector fields are then evaluated at the centroids of the triangular faces and thus yield piecewise constant color-coded images. For plotting purposes, the surface data is evaluated at the vertices of $\mathcal{S}_{h'}$ and interpolated piecewise linearly. Moreover, to simplify matters we plot piecewise linear approximation of the surfaces. We found that $\ell = 7$ iterative refinement steps sufficiently resolve the microscopy data.

In addition, we illustrate surface velocity fields with streamlines; see, e.g., [58]. Before doing so, the velocity fields are projected onto the x^1 - x^2 -plane. Then, given a steady vector field \mathbf{v} in the plane and a starting point x_0 , a streamline $\gamma(\cdot, x_0)$ solves the ordinary differential equation

$$(5.3) \quad \begin{aligned} \partial_\tau \gamma(\tau, x_0) &= \mathbf{v}(\gamma(\tau, x_0)), \\ \gamma(0, x_0) &= x_0. \end{aligned}$$

We compute numerical approximations γ_κ of (5.3) by solving

$$\begin{aligned} \gamma_\kappa(\tau + 1, x_0) &= \gamma_\kappa(\tau, x_0) + \kappa \mathbf{v}(\gamma_\kappa(\tau, x_0)), \\ \gamma_\kappa(0, x_0) &= x_0 \end{aligned}$$

for a given number of initial points $x_0 \in \mathbb{R}^2$ and for $\tau = 50$ iterations. Here, $\kappa > 0$ is a step size parameter that is set in dependence of \mathbf{v} . Moreover, we apply linear interpolation of \mathbf{v} . With increasing τ we adjust the color of γ_κ from yellow to green; see Figures 10 and 13. In what follows, for a given surface vector field $\hat{\mathbf{X}}$ we create a streamline visualization of its projection $P_{x^3}\hat{\mathbf{X}}$ onto the x^1 - x^2 -plane.

5.4. Results. We conducted several experiments with said zebrafish microscopy data. In a first step, we minimized functional (4.9) by solving the optimality conditions (4.13) to obtain an approximation of the deforming surface. We chose the parameter r of the Sobolev space $H^r(\mathcal{S}^2)$ as $r = 3 + \epsilon$, where $\epsilon = 2.2204 \cdot 10^{-16}$ is the machine precision. This particular choice originates from regularity requirements discussed in [36, sect. 4.3]. The regularization parameters were set to $\beta_0 = 10^{-4}$ and $\beta_1 = 100$, and the space $\mathcal{Q} \subset H^r(\mathcal{S}^2)$ was chosen as $\mathcal{Q} = \text{span}\{\tilde{Y}_{n,j} : n = 0, \dots, 10, j = 1, \dots, 2n + 1\}$.

Figure 5 depicts three selected frames of a minimizing function $\tilde{\rho}$ of \mathcal{G} computed for frames $\{100, 101, \dots, 151\}$ of the microscopy sequence. Figure 6 shows the estimated surface \mathcal{M}_t for the same frames together with the surface data \hat{f} , which is obtained by the radial maximum intensity projection (5.1) with $\epsilon = 0.1$. We highlight that the deformation of the embryo is well-captured and contains the anticipated cell features; cf. also the unprocessed volumetric

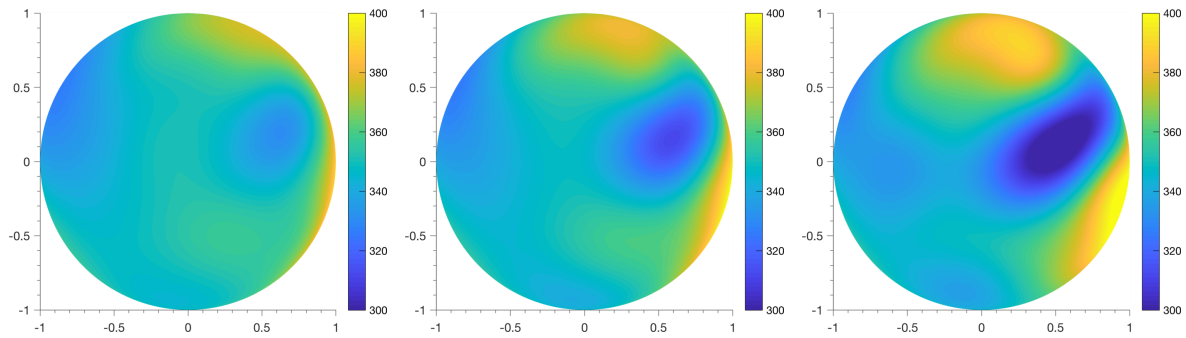


Figure 5. Depicted is a top view of the recovered (radius) function $\tilde{\rho}$ at times 110, 130, and 150 (from left to right). All dimensions are in micrometers (μm).

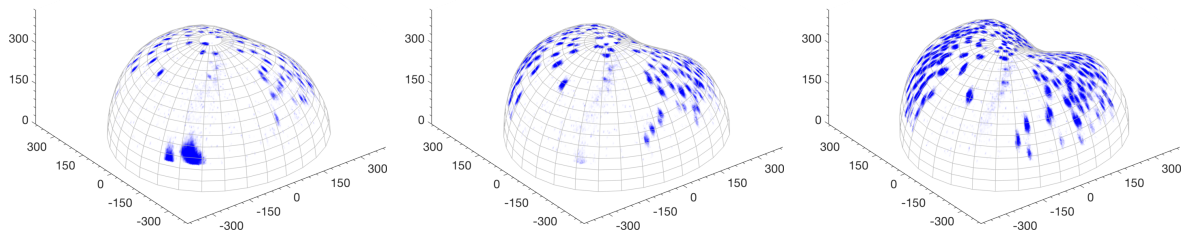


Figure 6. Shown are frames 110, 130, and 150 (from left to right) of the upper hemisphere of the estimated sphere-like surface \mathcal{M}_t together with surface data \hat{f} . The curved surface is indicated by an artificial mesh which—for illustration purposes—has been widened in the radial direction by one percent of its original distance from the origin. All dimensions are in micrometers (μm).

data in Figure 1. The growing dent in the surface corresponds to the clearly visible dark blue area in Figure 5. Moreover, Figure 7 illustrates a section of the unprocessed microscopy data f^δ together with the fitted surface (in grey) and the narrow band (in red and green) used in (5.1) and (5.2) to obtain the surface data \hat{f} and the gradient $\nabla_{\mathcal{M}}\hat{f}$ from the volumetric data f^δ , respectively. The fitted surface accurately represents the single-cell layer, and cell material is located almost entirely within the narrow band.

In a second step, we computed minimizers of the functionals (3.16) and (3.21) for one pair of frames by solving the corresponding optimality conditions (4.7) and (4.8), respectively. As outlined in section 4.6, the finite-dimensional subspace $\mathcal{U} \subset H^1(\mathcal{M}_t, T\mathcal{M}_t)$ in (4.4) was created by five mesh refinements resulting in approximately $N = 10^4$ (tangent) vectorial basis functions. Moreover, the parameters of the basis functions were set to $k = 3$ and $h = 0.99$. The degree of the numerical cubature was chosen as 400, yielding approximately 8600 evaluation points on the spherical cap. It remains to discuss the choice of the function s in the regularization functionals (3.17) and (3.22). We chose it in dependence of the surface data \hat{f} as

$$(5.4) \quad s := \begin{cases} 1 - \eta & \text{if } 1 - \eta < \hat{f}, \\ \hat{f} & \text{if } \eta \leq \hat{f} \leq 1 - \eta, \\ \eta & \text{if } \hat{f} < \eta, \end{cases}$$

with $\eta = 10^{-4}$. This guarantees that $s(t, \cdot) : \mathcal{M}_t \rightarrow (0, 1)$ so that (3.16) and (3.21) are well-posed minimization problems.

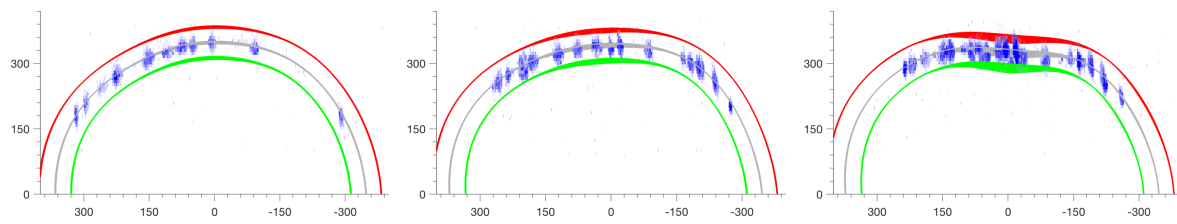


Figure 7. Shown are cross sections of $50\ \mu\text{m}$ thickness of the unprocessed microscopy data f^δ , the interpolated surface \mathcal{M}_t (in grey), and the narrow band (red and green) within which projection (5.1) is taken to obtain \hat{f} . The images correspond to those depicted in Figure 6, i.e., frames 110, 130, and 150 (from left to right). All dimensions are in micrometers (μm).

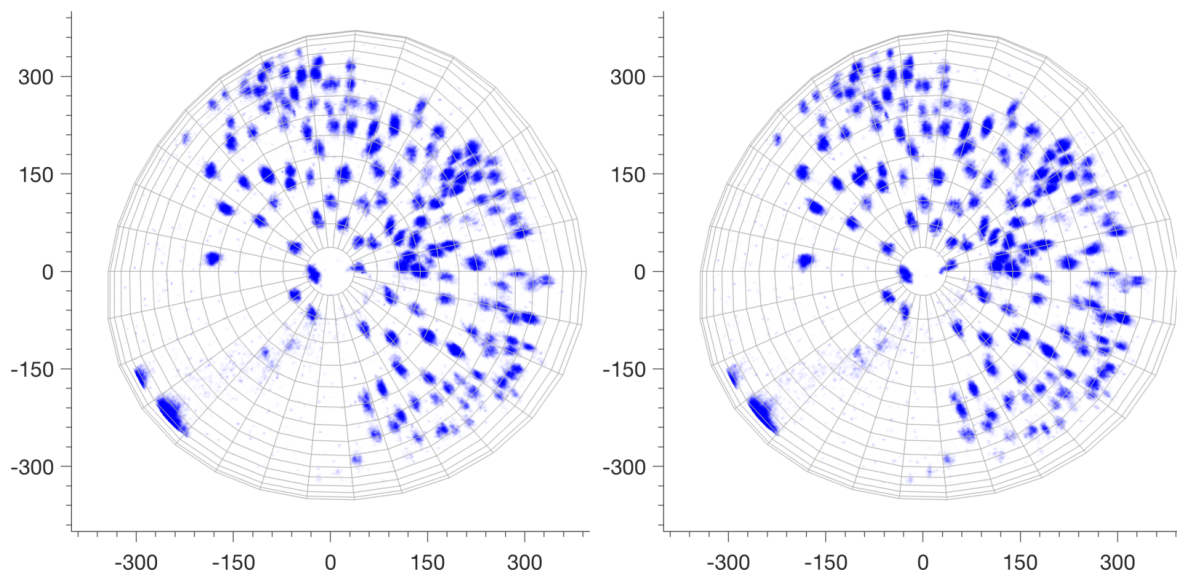


Figure 8. Frames 112 (left) and 113 (right) with a top view of the processed microscopy image sequence with an artificial mesh superimposed. The mesh has been widened by one percent of its radius for better illustration. All dimensions are in micrometers (μm).

All experiments were performed on an Intel Core i5-6500 3.20 GHz MacBook Pro equipped with 16 GB RAM. The running time was governed by the evaluation of the integrals in (4.7) and (4.8), which altogether amounts to approximately 150 seconds per pair of frames in our MATLAB implementation. In comparison to previous works [33, 36], where globally supported vectorial basis functions were used and computation time was several hours, this represents a significant speed-up. Furthermore, the memory requirements have been drastically reduced.

All systems of linear equations were solved by application of the backslash operator in MATLAB and resulted in a relative residual less than 10^{-14} within just a few seconds. Both the microscopy data¹ and the source code of the implementation² are available online.

Figure 8 depicts the two selected (consecutive) frames with a top view of the processed

¹<https://doi.org/10.5281/zenodo.1211599>.

²<https://doi.org/10.5281/zenodo.1238910>.

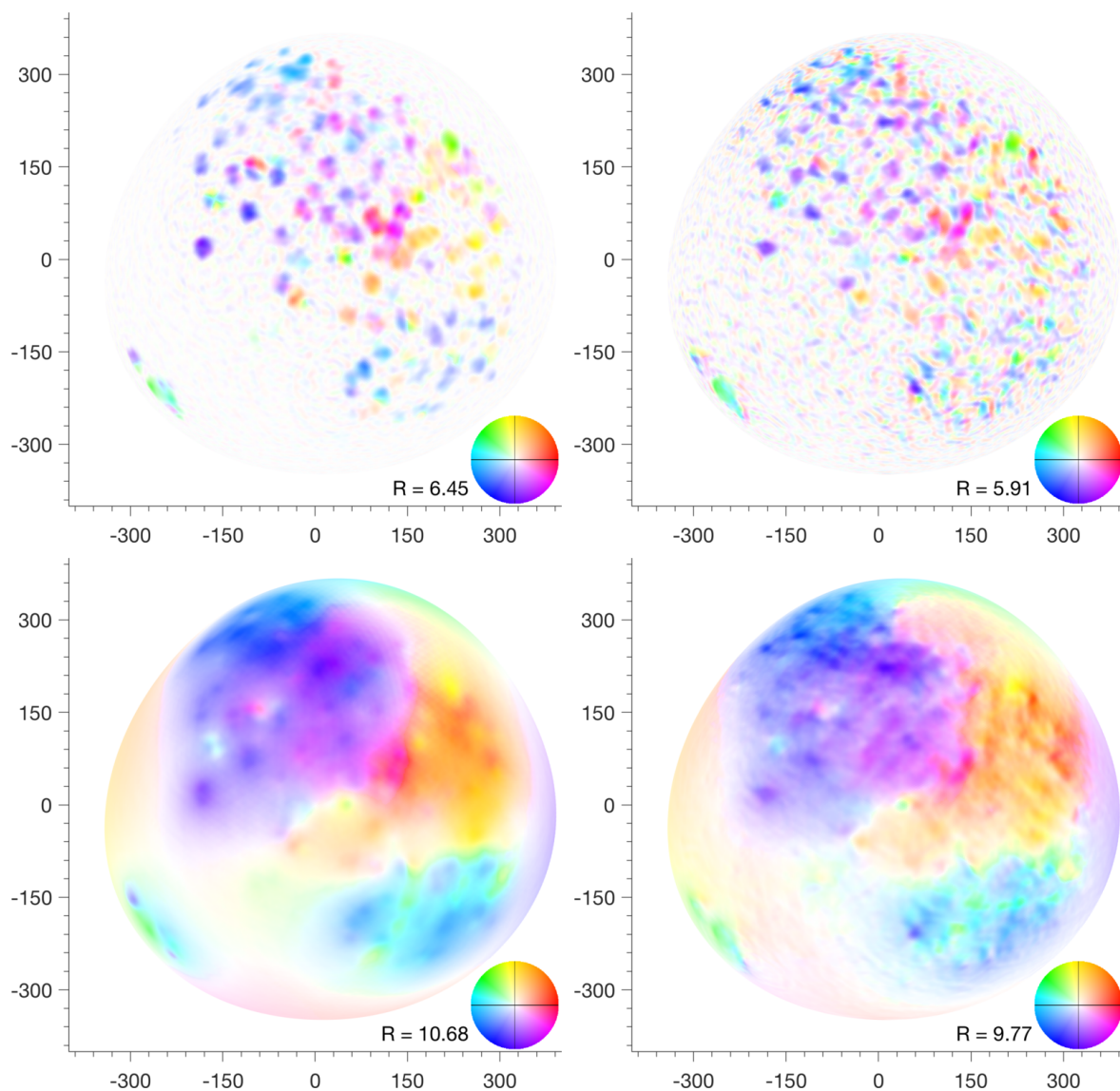


Figure 9. Color-coded visualization of minimizers $\hat{\mathbf{w}}$ of \mathcal{E} (left) and $\hat{\mathbf{u}}$ of \mathcal{F} (right), respectively, for two different choices of s . The top row shows s as defined in (5.4), while the bottom row illustrates the choice $s \equiv 1$. The regularization parameters were chosen as follows. Top left: $\alpha_0 = 10^{-1}$ and $\alpha_1 = 10^{-3}$. Top right: $\alpha_0 = 10^{-1}$, $\alpha_1 = 10^{-3}$, and $\alpha_2 = 10^{-3}$. Bottom left and bottom right: $\alpha_0 = 10^{-1}$. All dimensions are in micrometers (μm).

microscopy image sequence. All results in the following figures were computed for this particular pair of frames and are also shown from a top view only. In Figure 9 we portray minimizers $\hat{\mathbf{w}}$ and $\hat{\mathbf{u}}$ of functionals \mathcal{E} and \mathcal{F} , respectively. Moreover, we compare the effect of two different choices of s . While the top row shows results for s chosen as in (5.4) and indicates that individual motion of cells is captured particularly well by the proposed model, the bottom row depicts results for $s \equiv 1$. While the choice $s \equiv 1$ provides a better insight into

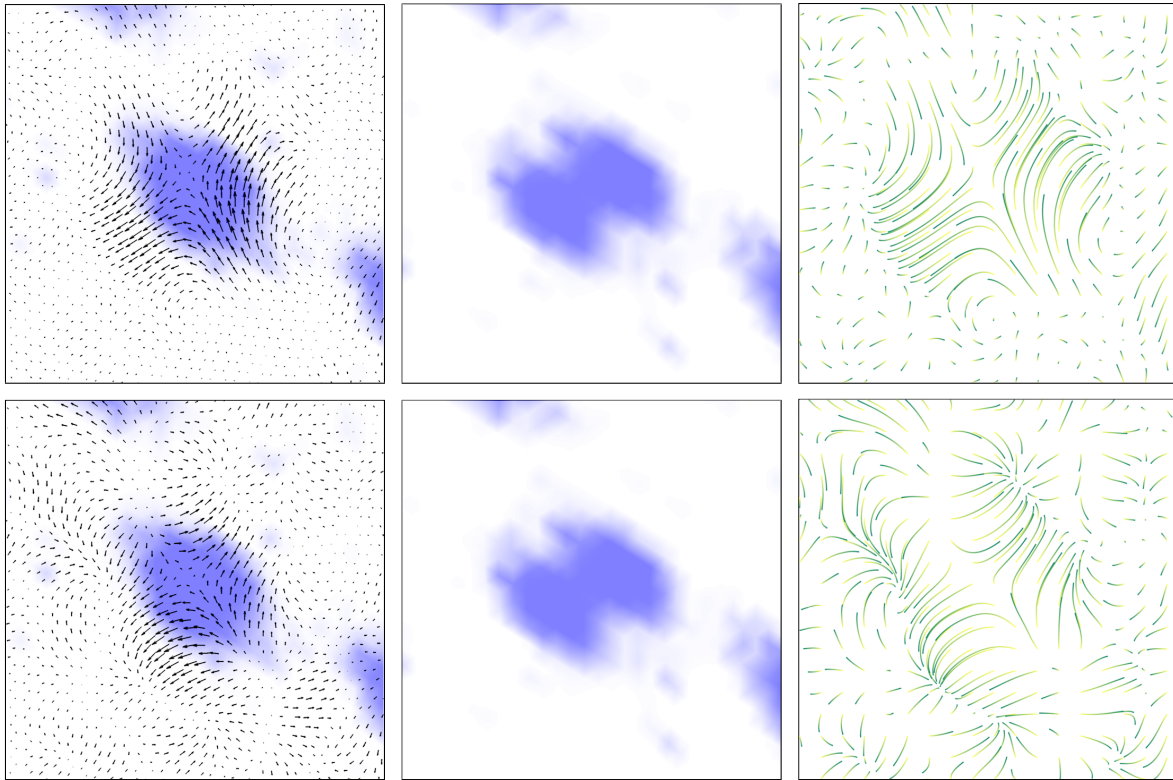


Figure 10. Detailed view of estimated velocities $\hat{\mathbf{w}}$ (top) and $\hat{\mathbf{u}}$ (bottom) during a cell division. Depicted are the surface data \hat{f} at frame $t = 112$ with the respective velocity superimposed (left), the data \hat{f} at frame $t = 113$ (middle), and the streamline representation of the respective velocity (right), as outlined in section 5.3. The same parameters as in Figure 9 (top row) were used. For better illustration, \hat{f} has been brightened slightly.

the collective motion of cells on a global scale, the spatially dependent s captures individual cell movements (visually) more accurately. Note also the difference in the magnitude, which is indicated by the radius R of the (scaled) color disk. For $s \equiv 1$, the minimizers $\hat{\mathbf{w}}$ and $\hat{\mathbf{u}}$ are visually similar, whereas for s chosen as in (5.4) they differ significantly. In particular, note the oscillations where no cell material is present. In our experiments we found that these are due to noise in the data and can be suppressed by larger choices of α_2 without changing the result substantially.

Figure 10 depicts a detailed section of the velocity fields shown in Figure 9 (top row) during a cell division. Clearly, the cell division is adequately captured and the velocity fields are spatially confined. Notice also the differences in the streamline plot.

In Figure 11, we illustrate tangent vector fields obtained for increasing regularization parameter α_0 for s chosen as in (5.4). Observe in both rows the broadening of the support and the decrease in magnitude of the velocity fields for increasing α_0 .

Moreover, Figure 12 depicts minimizers for increasing parameter α_0 for $s \equiv 1$. As expected, the velocity fields become more regular with increasing α_0 and, due to the regularization functional being a norm, decrease in magnitude. These findings are in line with the results

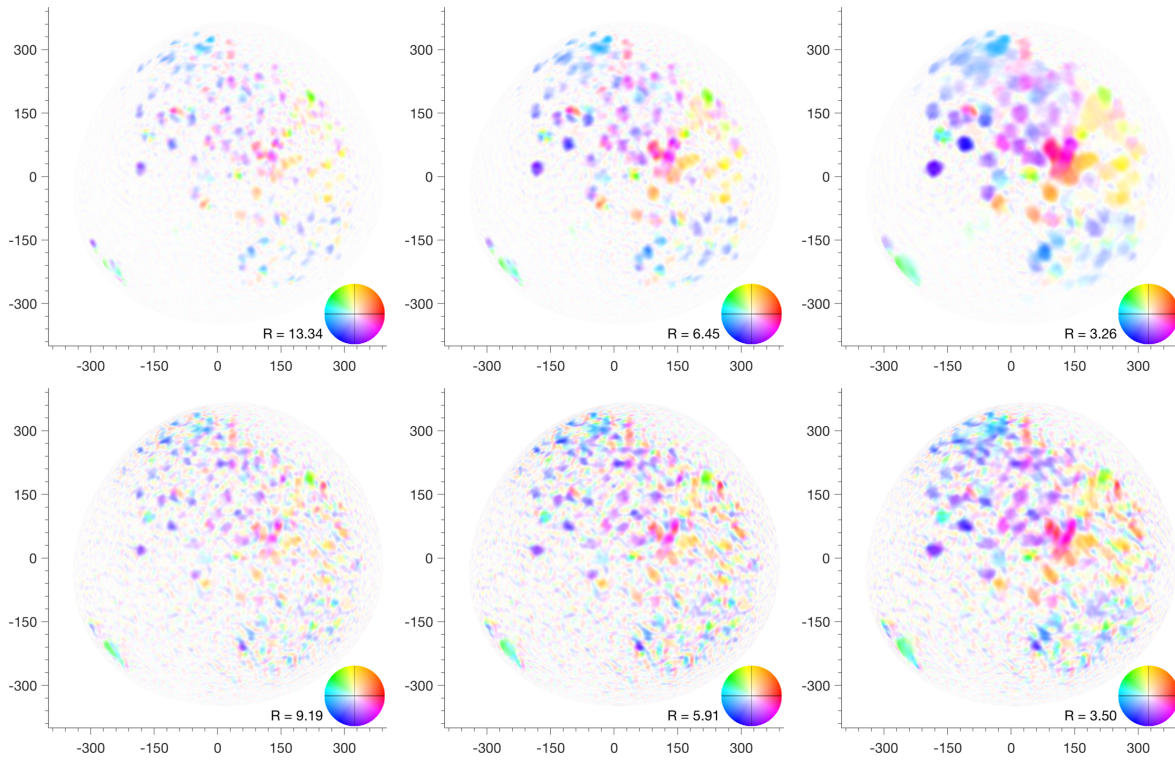


Figure 11. Computed tangent vector fields $\hat{\mathbf{w}}$ (top) and $\hat{\mathbf{u}}$ (bottom) for increasing regularization parameter $\alpha_0 = 10^{-2}$ (left), $\alpha_0 = 10^{-1}$ (middle), and $\alpha_0 = 1$ (right). The other parameters were kept fixed as $\alpha_1 = 10^{-3}$ and $\alpha_2 = 10^{-3}$. The function s was set as in (5.4).

obtained in [33, 36]. In Figure 13, we visualize the velocity fields from Figure 12 with the help of streamlines as outlined in section 5.3.

We also illustrate the total velocity $\hat{\mathbf{U}}$ of cells. Recall from section 3 that for estimated velocity fields $\hat{\mathbf{w}}$ and $\hat{\mathbf{u}}$, it can be computed as $\hat{\mathbf{U}} = \hat{\mathbf{V}} + \hat{\mathbf{w}}$ (respectively as $\hat{\mathbf{U}} = V\hat{\mathbf{N}} + \hat{\mathbf{u}}$). From (2.1) it follows that the surface velocity is given by $\hat{\mathbf{V}} = \partial_t \mathbf{y} = \partial_t \tilde{\rho} \mathbf{x}$, which points in the radial direction. In Figure 14, we compare the total velocities obtained for the velocity fields shown in Figure 9 (top row). First, observe the minor differences between $\hat{\mathbf{V}}$ and $V\hat{\mathbf{N}}$, indicating that the surface velocity points mainly in the normal direction. Second, note the significant difference in the magnitudes. As a result, the surface movement is almost negligible for the considered data.

6. Conclusions. With the goal of efficient motion estimation in volumetric microscopy data, we followed the paradigm of dimensional reduction and considered brightness and mass conservation on evolving sphere-like surfaces. We derived a generalized continuity equation valid for time-varying surfaces embedded in Euclidean 3-space and discussed its relation to the generalized optical flow equation derived in [34]. In light of the ill-posedness of the discussed conservation laws, we proposed the use of spatially-varying regularization functionals suited for considered microscopy data of fluorescently labeled cells. For the efficient numerical solution, we devised a Galerkin method based on compactly supported (tangent) vectorial

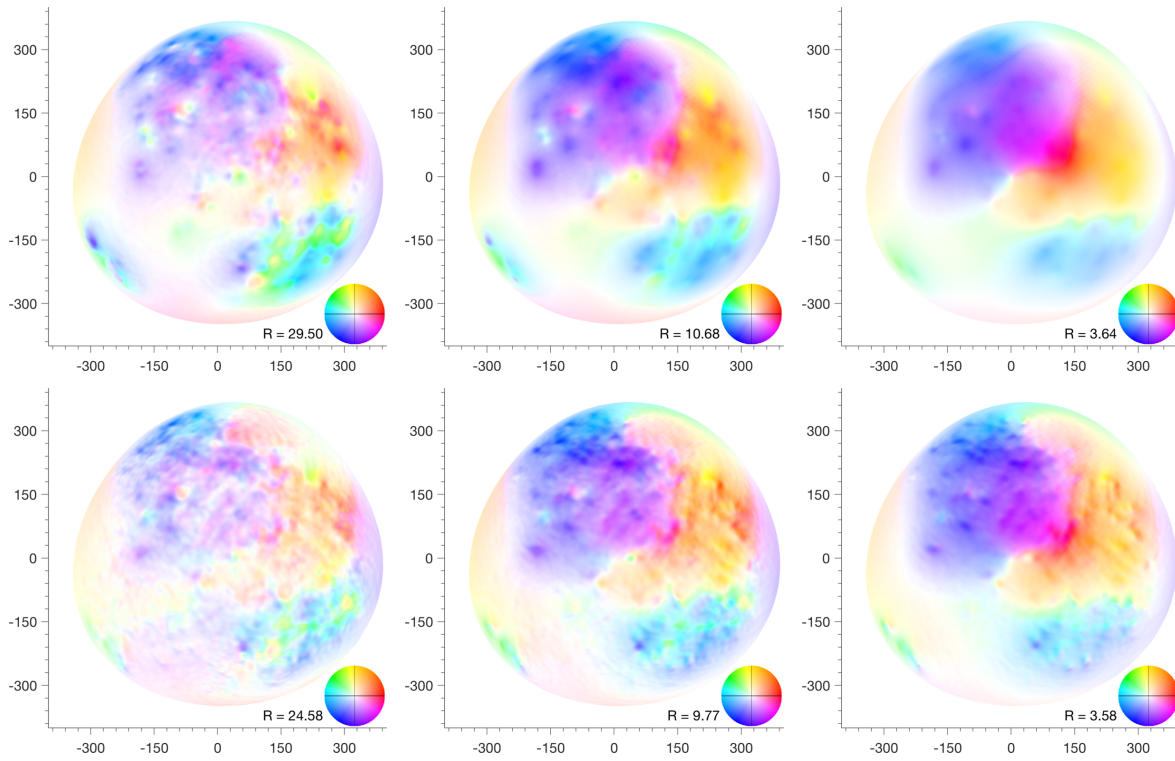


Figure 12. Computed tangent vector fields $\hat{\mathbf{w}}$ (top) and $\hat{\mathbf{u}}$ (bottom) for increasing regularization parameter $\alpha_0 = 10^{-2}$ (left), $\alpha_0 = 10^{-1}$ (middle), and $\alpha_0 = 1$ (right). The other parameters were kept fixed as $\alpha_1 = 10^{-3}$ and $\alpha_2 = 10^{-3}$. The function s was set to $s \equiv 1$.

basis functions allowing for efficient evaluation of the optimality conditions. A significant performance improvement was observed compared to previous methods based on globally supported basis functions. In order to accurately estimate the velocity of the (artificially) imposed sphere-like surface, we considered surface interpolation with spatial and temporal regularization. We performed several experiments on the basis of the aforementioned zebrafish microscopy data. The computed velocity fields indicate that cell motion can be estimated well and efficiently with the proposed method. However, it is left for future research to evaluate the considered models quantitatively and to investigate theoretical guarantees of the proposed numerical method.

Appendix A. Hilbert–Schmidt norm of the covariant derivative. In the following, we derive a coordinate representation of the Hilbert–Schmidt norm of the covariant derivative (2.8). The Riemannian metric $g = (g_{ij})$ is a covariant symmetric $(0, 2)$ -tensor, and its inverse $g^{-1} = (g^{ij})$ is a contravariant symmetric $(2, 0)$ -tensor. Both obey a transformation law when changing from one basis to another. Let $\{\hat{\mathbf{e}}_1, \hat{\mathbf{e}}_2\}$ be an arbitrary basis of $T_x \mathcal{M}_t$ at $x \in \mathcal{M}_t$ such that

$$(A.1) \quad \hat{\mathbf{e}}_i = \alpha_i^j \partial_j \mathbf{y}.$$

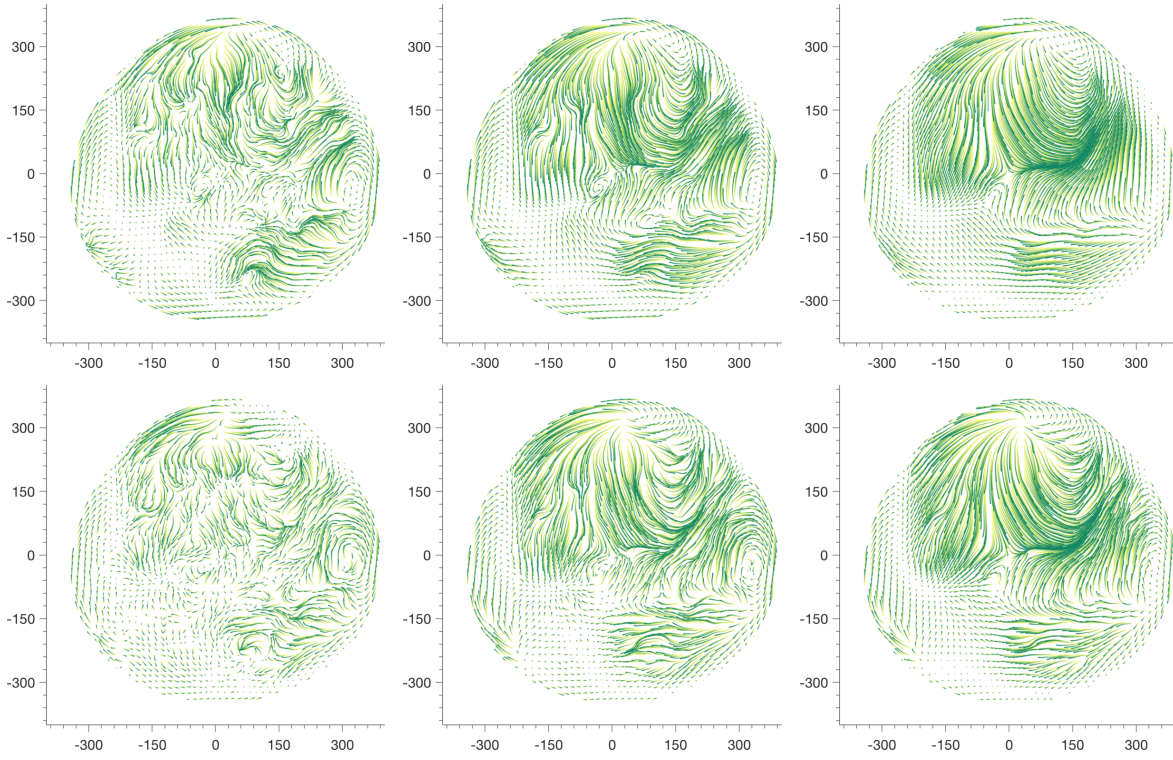


Figure 13. Shown are streamlines visualizing the velocity fields from Figure 12, i.e., velocity fields obtained for increasing regularization parameter α_0 (from left to right). The top row shows streamlines computed for $P_{x3}\hat{\mathbf{w}}$, while the bottom row illustrates them for $P_{x3}\hat{\mathbf{u}}$. The change in color from yellow to green illustrates the increasing parameter τ .

Here, the entries (α_i^j) form a matrix with inverse $(\alpha^{-1})_i^j$. Then, for a (p, q) -tensor $T_{j_1, \dots, j_q}^{i_1, \dots, i_p}$ of order $p + q$, which is defined in the basis $\{\partial_1 \mathbf{y}, \partial_2 \mathbf{y}\}$, its representation in the basis $\{\hat{\mathbf{e}}_1, \hat{\mathbf{e}}_2\}$ is given by

$$(A.2) \quad \mathfrak{T}_{j'_1, \dots, j'_q}^{i'_1, \dots, i'_p} = (\alpha^{-1})_{i'_1}^{j'_1} \dots (\alpha^{-1})_{i'_p}^{j'_p} T_{j_1, \dots, j_q}^{i_1, \dots, i_p} \alpha_{j'_1}^{j_1} \dots \alpha_{j'_q}^{j_q}.$$

See, e.g., [37] for details. With this at hand we can show the following.

Lemma A.1. *Let $t \in I$ and $x = \mathbf{y}(t, \xi)$ be arbitrary for some $\xi \in \Omega$. Then, for $\hat{\mathbf{v}} = v^i \partial_i \mathbf{y}$, it holds that*

$$(A.3) \quad \|\nabla \hat{\mathbf{v}}\|_2^2 = g_{kl} g^{ij} D_i v^k D_j v^l,$$

where we have omitted the arguments (t, x) on the left-hand side and (t, ξ) on the right-hand side.

Proof. First, let us show that the right-hand side of (A.3) is parametrization independent. To this end, let $\{\partial_1 \mathbf{y}, \partial_2 \mathbf{y}\}$ and $\{\hat{\mathbf{e}}_1, \hat{\mathbf{e}}_2\}$ be arbitrary bases for $T_x \mathcal{M}_t$ such that its relation is given by (A.1). Then, by [37, Lemma 4.7] and (A.2), we have the transformation law

$$\mathfrak{D}_i v^k = (\alpha^{-1})_s^k D_t v^s \alpha_i^t$$

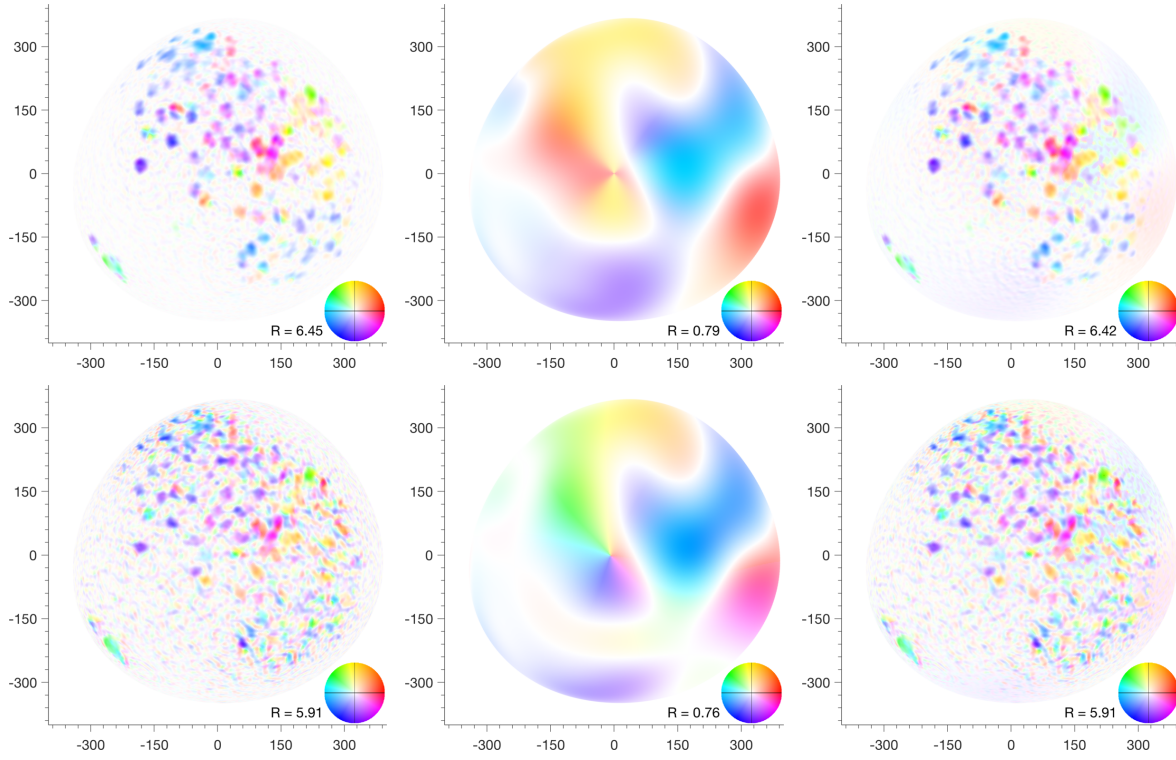


Figure 14. The top row depicts the velocity $\hat{\mathbf{w}}$ (left), the surface velocity $\hat{\mathbf{V}}$ (middle), and the total velocity estimated as $\hat{\mathbf{V}} + \hat{\mathbf{w}}$ (right). The bottom row depicts the velocity $\hat{\mathbf{u}}$ (left), the normal component $V\hat{\mathbf{N}}$ (middle), and the total velocity estimated as $V\hat{\mathbf{N}} + \hat{\mathbf{u}}$ (right). The same parameters as in Figure 9 (top row) were used.

for the components (4.6) of the covariant derivative. Moreover, (g_{ij}) and (g^{ij}) transform as $g_{kl} = g_{mn}\alpha_k^m\alpha_l^n$ and $g^{ij} = (\alpha^{-1})_p^i(\alpha^{-1})_q^jg^{pq}$, respectively. Recall that, by definition, $\alpha_i^k(\alpha^{-1})_k^j = \delta_i^j$ and $(\alpha^{-1})_i^k\alpha_k^j = \delta_i^j$. As a consequence,

$$\begin{aligned} g_{kl}g^{ij}\mathcal{D}_i\mathbf{v}^k\mathcal{D}_j\mathbf{v}^\ell &= g_{mn}\alpha_k^m\alpha_l^n(\alpha^{-1})_p^i(\alpha^{-1})_q^jg^{pq}(\alpha^{-1})_s^kD_tv^s\alpha_i^t(\alpha^{-1})_u^\ell D_wv^u\alpha_j^w \\ &= g_{mn}g^{pq}D_tv^sD_wv^u\delta_s^m\delta_u^n\delta_p^t\delta_q^w \\ &= g_{mn}g^{pq}D_pv^mD_qv^n. \end{aligned}$$

Suppose now that $\{\hat{\mathbf{e}}_1, \hat{\mathbf{e}}_2\}$ is orthonormal so that $\mathbf{g} = (\delta_{ij})$ and $\mathbf{g}^{-1} = (\delta^{ij})$. Then,

$$g_{kl}g^{ij}\mathcal{D}_i\mathbf{v}^k\mathcal{D}_j\mathbf{v}^\ell = \sum_{i,k}(\mathcal{D}_i\mathbf{v}^k)^2 = \sum_i\|\nabla_{\hat{\mathbf{e}}_i}\hat{\mathbf{v}}\|^2 = \|\nabla\hat{\mathbf{v}}\|_2^2,$$

where the second equality follows from the fact that

$$\sum_i\|\nabla_{\hat{\mathbf{e}}_i}\hat{\mathbf{v}}\|^2 = \sum_i\mathcal{D}_i\mathbf{v}^k\hat{\mathbf{e}}_k \cdot \mathcal{D}_i\mathbf{v}^\ell\hat{\mathbf{e}}_\ell = \sum_i\delta_{kl}\mathcal{D}_i\mathbf{v}^k\mathcal{D}_i\mathbf{v}^\ell = \sum_{i,k}(\mathcal{D}_i\mathbf{v}^k)^2,$$

and the last equality is by definition (2.8). The claim follows from combining these equations. ■

Acknowledgments. The author thanks Pia Aanstad for kindly providing the microscopy data. Moreover, he is grateful to Peter Elbau, Christian Gerhards, and Clemens Kirisits for their helpful comments.

REFERENCES

- [1] F. AMAT, W. LEMON, D. P. MOSSING, K. MCDOLE, Y. WAN, K. BRANSON, E. W. MYERS, AND P. J. KELLER, *Fast, accurate reconstruction of cell lineages from large-scale fluorescence microscopy data*, Nat. Meth., 11 (2014), pp. 951–958.
- [2] F. AMAT, E. W. MYERS, AND P. J. KELLER, *Fast and robust optical flow for time-lapse microscopy using super-voxels*, Bioinformatics, 29 (2013), pp. 373–380.
- [3] A. A. AMINI, *A scalar function formulation for optical flow*, in Proceedings of the 3rd European Conference on Computer Vision, J.-O. Eklundh, ed., vol. 1, Springer, Berlin, 1994, pp. 123–131.
- [4] G. AUBERT, R. DERICHE, AND P. KORNPBST, *Computing optical flow via variational techniques*, SIAM J. Appl. Math., 60 (1999), pp. 156–182, <https://doi.org/10.1137/S0036139998340170>.
- [5] G. AUBERT AND P. KORNPBST, *Mathematical Problems in Image Processing. Partial Differential Equations and the Calculus of Variations*, 2nd ed., Appl. Math. Sci. 147, Springer, New York, 2006.
- [6] S. BAKER, D. SCHARSTEIN, J. P. LEWIS, S. ROTH, M. J. BLACK, AND R. SZELISKI, *A database and evaluation methodology for optical flow*, Int. J. Comput. Vis., 92 (2011), pp. 1–31.
- [7] L. BAR, T. F. CHAN, G. CHUNG, M. JUNG, N. KIRYATI, R. MOHIEDDINE, N. SOCHEN, AND L. A. VESE, *Mumford and Shah model and its applications to image segmentation and image restoration*, in Handbook of Mathematical Methods in Imaging, O. Scherzer, ed., Springer, New York, 2011, pp. 1095–1157.
- [8] M. BAUER, M. GRASMAIR, AND C. KIRISITS, *Optical flow on moving manifolds*, SIAM J. Imaging Sci., 8 (2015), pp. 484–512, <https://doi.org/10.1137/140965235>.
- [9] D. BÉRÉZIAT, I. HERLIN, AND L. YOUNES, *A generalized optical flow constraint and its physical interpretation*, in Proceedings of the IEEE Conference on Computer Vision and Pattern Recognition, vol. 2, IEEE Press, Piscataway, NJ, 2000, pp. 487–492.
- [10] K. BORIC, P. ORIO, T. VIÉVILLE, AND K. WHITLOCK, *Quantitative analysis of cell migration using optical flow*, PLOS One, 8 (2013), pp. 1–11.
- [11] M. BOTSCH, L. KOBELT, M. PAULY, P. ALLIEZ, AND B. LÉVY, *Polygon Mesh Processing*, CRC Press, Boca Raton, FL, 2010.
- [12] P. CERMELLI, E. FRIED, AND M. E. GURTIN, *Transport relations for surface integrals arising in the formulation of balance laws for evolving fluid interfaces*, J. Fluid Mech., 544 (2005), pp. 339–351.
- [13] T. CORPETTI, D. HEITZ, G. ARROYO, É. MÉMIN, AND A. SANTA-CRUZ, *Fluid experimental flow estimation based on an optical-flow scheme*, Expe. Fluids, 40 (2006), pp. 80–97.
- [14] T. CORPETTI, É. MÉMIN, AND P. PÉREZ, *Dense estimation of fluid flows*, IEEE Trans. Pattern Anal. Mach. Intell., 24 (2002), pp. 365–380.
- [15] M. DAWOOD, C. BRUNE, O. SCHOBER, M. SCHÄFERS, AND K. P. SCHÄFERS, *A continuity equation based optical flow method for cardiac motion correction in 3D PET data*, in Medical Imaging and Augmented Reality, H. Liao, P. J. Edwards, X. Pan, Y. Fan, and G.-Z. Yang, eds., Lecture Notes in Comput. Sci. 6326, Springer, Berlin, 2010, pp. 88–97.
- [16] H. DIRKS, *Variational Methods for Joint Motion Estimation and Image Reconstruction*, Ph.D. thesis, Institute for Computational and Applied Mathematics, University of Münster, Germany, 2015.
- [17] M. P. DO CARMO, *Differential Geometry of Curves and Surfaces*, Prentice-Hall, Englewood Cliffs, NJ, 1976.
- [18] M. P. DO CARMO, *Riemannian Geometry*, Birkhäuser, Basel, 1992.
- [19] G. DZIUK AND C. M. ELLIOTT, *Finite element methods for surface PDEs*, Acta Numer., 22 (2013), pp. 289–396.
- [20] W. FREEDEN AND M. SCHREINER, *Non-orthogonal expansions on the sphere*, Math. Methods Appl. Sci., 18 (1995), pp. 83–120.
- [21] E. HEBEY, *Sobolev Spaces on Riemannian Manifolds*, Lecture Notes in Math. 1635, Springer-Verlag, Berlin, 1996.

- [22] I. HEEMSKERK AND S. J. STREICHAN, *Tissue cartography: Compressing bio-image data by dimensional reduction*, Nat. Meth., 12 (2015), pp. 1139–1142.
- [23] D. HEITZ, E. MÉMIN, AND CH. SCHNÖRR, *Variational fluid flow measurements from image sequences: Synopsis and perspectives*, Expe. Fluids, 48 (2010), pp. 369–393.
- [24] K. HESSE, I. H. SLOAN, AND R. S. WOMERSLEY, *Numerical integration on the sphere*, in Handbook of Geomathematics, W. Freeden, M. Z. Nashed, and T. Sonar, eds., Springer, New York, 2010, pp. 1187–1219.
- [25] M. W. HIRSCH, *Differential Topology*, Grad. Texts in Math. 33, Springer-Verlag, New York, 1994.
- [26] B. K. P. HORN AND B. G. SCHUNCK, *Determining optical flow*, Artificial Intelligence, 17 (1981), pp. 185–203.
- [27] A. IMIYA, H. SUGAYA, A. TORII, AND Y. MOCHIZUKI, *Variational analysis of spherical images*, in Computer Analysis of Images and Patterns, Lecture Notes in Comput. Sci. 3691, A. Gagalowicz and W. Philips, eds., Springer, Berlin, 2005, pp. 104–111.
- [28] P. J. KELLER, *Imaging morphogenesis: Technological advances and biological insights*, Science, 340 (2013), 1234168.
- [29] P. J. KELLER, A. D. SCHMIDT, A. SANTELLA, K. KHAIRY, Z. BAO, J. WITTBRODT, AND E. H. K. STELZER, *Fast, high-contrast imaging of animal development with scanned light sheet-based structured-illumination microscopy*, Nat. Meth., 7 (2010), pp. 637–642.
- [30] P. J. KELLER, A. D. SCHMIDT, J. WITTBRODT, AND E. H. K. STELZER, *Reconstruction of zebrafish early embryonic development by scanned light sheet microscopy*, Science, 322 (2008), pp. 1065–1069.
- [31] C. B. KIMMEL, W. W. BALLARD, S. R. KIMMEL, B. ULLMANN, AND T. F. SCHILLING, *Stages of embryonic development of the zebrafish*, Devel. Dyn., 203 (1995), pp. 253–310.
- [32] C. KIRISITS, L. F. LANG, AND O. SCHERZER, *Optical flow on evolving surfaces with an application to the analysis of 4D microscopy data*, in Proceedings of the Fourth International Conference on Scale Space and Variational Methods in Computer Vision (SSVM '13) A. Kuijper, K. Bredies, T. Pock, and H. Bischof, eds., Lecture Notes in Comput. Sci. 7893, Springer-Verlag, Berlin, 2013, pp. 246–257.
- [33] C. KIRISITS, L. F. LANG, AND O. SCHERZER, *Decomposition of optical flow on the sphere*, GEM. Int. J. Geomath., 5 (2014), pp. 117–141.
- [34] C. KIRISITS, L. F. LANG, AND O. SCHERZER, *Optical flow on evolving surfaces with space and time regularisation*, J. Math. Imaging Vision, 52 (2015), pp. 55–70.
- [35] U. KRZIC, S. GUNTHER, T. E. SAUNDERS, S. J. STREICHAN, AND L. H. HUFNAGEL, *Multiview light-sheet microscope for rapid in toto imaging*, Nat. Meth., 9 (2012), pp. 730–733.
- [36] L. F. LANG AND O. SCHERZER, *Optical flow on evolving sphere-like surfaces*, Inverse Probl. Imaging, 11 (2017), pp. 305–338.
- [37] J. M. LEE, *Riemannian Manifolds. An Introduction to Curvature*, Grad. Texts in Math. 176, Springer-Verlag, New York, 1997.
- [38] J. M. LEE, *Introduction to Smooth Manifolds*, 2nd ed., Grad. Texts in Math. 218, Springer, New York, 2013.
- [39] J. LEFÈVRE AND S. BAILLET, *Optical flow and advection on 2-Riemannian manifolds: A common framework*, IEEE Trans. Pattern Anal. Mach. Intell., 30 (2008), pp. 1081–1092.
- [40] S. G. MEGASON AND S. E. FRASER, *Digitizing life at the level of the cell: High-performance laser-scanning microscopy and image analysis for in toto imaging of development*, Mech. Dev., 120 (2003), pp. 1407–1420.
- [41] C. MELANI, M. CAMPANA, B. LOMBARDOT, B. RIZZI, F. VERONESI, C. ZANELLA, P. BOURGINE, K. MIKULA, N. PEYRIÉRAS, AND A. SARTI, *Cells tracking in a live zebrafish embryo*, in Proceedings of the 29th Annual International Conference of the IEEE Engineering in Medicine and Biology Society (EMBS 2007), IEEE Press, Piscataway, NJ, 2007, pp. 1631–1634.
- [42] V. MICHEL, *Lectures on Constructive Approximation. Fourier, Spline, and Wavelet Methods on the Real Line, the Sphere, and the Ball*, Birkhäuser, Basel, 2013.
- [43] S. NAIR AND T. F. SCHILLING, *Chemokine signaling controls endodermal migration during zebrafish gastrulation*, Science, 322 (2008), pp. 89–92.
- [44] P. QUELHAS, A. M. MENDONÇA, AND A. CAMPILHO, *Optical flow based Arabidopsis thaliana root meristem cell division detection*, in Image Analysis and Recognition, A. Campilho and M. Kamel, eds., Lecture Notes in Comput. Sci. 6112, Springer, Berlin, 2010, pp. 217–226.

- [45] E. G. REYNAUD, J. PEYCHL, J. HUISKEN, AND P. TOMANCAK, *Guide to light-sheet microscopy for adventurous biologists*, Nat. Meth., 12 (2014), pp. 30–34.
- [46] M. E. ROGNES, D. A. HAM, C. J. COTTER, AND A. T. T. MCRAE, *Automating the solution of PDEs on the sphere and other manifolds in FEniCS 1.2*, Geosci. Model Dev., 6 (2013), pp. 2099–2119.
- [47] B. SCHMID, G. SHAH, N. SCHERF, M. WEBER, K. THIERBACH, C. CAMPOS PÉREZ, I. ROEDER, P. AANSTAD, AND J. HUISKEN, *High-speed panoramic light-sheet microscopy reveals global endodermal cell dynamics*, Nat. Commun., 4 (2013), 2207.
- [48] CH. SCHNÖRR, *Determining optical flow for irregular domains by minimizing quadratic functionals of a certain class*, Int. J. Comput. Vis., 6 (1991), pp. 25–38.
- [49] M. SCHREINER, *Locally supported kernels for spherical spline interpolation*, J. Approx. Theory, 89 (1997), pp. 172–194.
- [50] B. G. SCHUNCK, *The motion constraint equation for optical flow*, in Proceedings of the 7th International Conference on Pattern Recognition, IEEE, New York, 1984, pages 29–22.
- [51] S. M. SONG AND R. M. LEAHY, *Computation of 3-D velocity fields from 3-D cine CT images of a human heart*, IEEE Trans. Med. Imag., 10 (1991), pp. 295–306.
- [52] A. TORII, A. IMIYA, H. SUGAYA, AND Y. MOCHIZUKI, *Optical flow computation for compound eyes: Variational analysis of omni-directional views*, in Brain, Vision, and Artificial Intelligence, Lecture Notes in Comput. Sci. 3704, M. De Gregorio, V. Di Maio, M. Frucci, and C. Musio, eds., Springer, Berlin, 2005, pp. 527–536.
- [53] H. TRIEBEL, *Theory of Function Spaces. II*, Monogr. Math. 84, Birkhäuser Verlag, Basel, 1992.
- [54] R. M. WARGA AND C. NÜSSLEIN-VOLHARD, *Origin and development of the zebrafish endoderm*, Development, 126 (1999), pp. 827–838.
- [55] J. WEICKERT, A. BRUHN, T. BROX, AND N. PAPENBERG, *A survey on variational optic flow methods for small displacements*, in Mathematical Models for Registration and Applications to Medical Imaging, O. Scherzer, ed., Math. Ind. 10, Springer, Berlin, 2006, pp. 103–136.
- [56] J. WEICKERT AND CH. SCHNÖRR, *A theoretical framework for convex regularizers in PDE-based computation of image motion*, Int. J. Comput. Vis., 45 (2001), pp. 245–264.
- [57] J. WEICKERT AND CH. SCHNÖRR, *Variational optic flow computation with a spatio-temporal smoothness constraint*, J. Math. Imaging Vision, 14 (2001), pp. 245–255.
- [58] D. WEISKOPF AND G. ERLEBACHER, *Overview of flow visualization*, in The Visualization Handbook, C. D. Hansen and C. R. Johnson, eds., Elsevier, Amsterdam, 2005, pp. 261–278.
- [59] R. P. WILDES, M. J. AMABILE, A. M. LANZILLOTTO, AND T.-S. LEU, *Recovering estimates of fluid flow from image sequence data*, Comput. Vision Image Understanding, 80 (2000), pp. 246–266.
- [60] L. ZHOU, C. KAMBHAMETTU, AND D. B. GOLDFOG, *Fluid structure and motion analysis from multi-spectrum 2D cloud image sequences*, in Proceedings of the IEEE Conference on Computer Vision and Pattern Recognition, vol. 2, IEEE Press, Piscataway, NJ, 2000, pp. 744–751.